



A full-coverage satellite-based global atmospheric CO₂ dataset at 0.05° resolution from 2015 to 2021 for exploring global carbon dynamics

Zhige $Wang^{1,2,3}$, Ce $Zhang^{4,5}$, Kejian Shi 6 , Yulin Shangguan 1,2 , Bifeng $Hu^{7,8}$, Xueyao Chen 1,2,9 , Danqing $Wei^{1,2,10}$, Songchao Chen 1,2,11 , Peter M. Atkinson 12,13 , and Qiang $Zhang^3$

State Key Laboratory of Soil Pollution Control and Safety, Zhejiang University, Hangzhou, 310058, China
 College of Environmental and Resource Sciences, Zhejiang University, Hangzhou 310058, China
 Ministry of Education Key Laboratory for Earth System Modeling, Department of Earth System Science,
 Tsinghua University, Beijing 100084, China

⁴School of Geographical Sciences, University of Bristol, Bristol BS8 1SS, UK
 ⁵UK Centre for Ecology & Hydrology, Library Avenue, Bailrigg, Lancaster LA1 4AP, UK
 ⁶School of Geographical Sciences, Faculty of Science and Engineering,

 University of Nottingham Ningbo China, Ningbo 315100, China

 ⁷Department of Land Resource Management, School of Public Administration,

 Jiangxi University of Finance and Economics, Nanchang, 330013, China

 ⁸Key Laboratory of Data Science in Finance and Economics of Jiangxi Province, Jiangxi University of Finance and Economics, Nanchang, 330013, China

Correspondence: Songchao Chen (chensongchao@zju.edu.cn)

Received: 24 July 2024 – Discussion started: 25 October 2024 Revised: 2 June 2025 – Accepted: 28 July 2025 – Published: 15 October 2025

Abstract. The irreversible trend for global warming underscores the necessity for accurate monitoring and analysis of atmospheric carbon dynamics on a global scale. Carbon satellites hold significant potential for atmospheric CO₂ monitoring. However, existing studies on global CO₂ are constrained by coarse resolution (ranging from 0.25 to 2°) and limited spatial coverage. In this study, we developed a new global dataset of column-averaged dry-air mole fraction of CO₂ (XCO₂) at 0.05° resolution with full coverage using carbon satellite observations, multi-source satellite products, and an improved deep learning model. We then investigated changes in global atmospheric CO₂ and anomalies from 2015 to 2021. The reconstructed XCO₂ products show a better agreement with Total Carbon Column Observing Network (TCCON) measurements, with R^2 of 0.92 and RMSE of 1.54 ppm. The products also provide more accurate information on the global and regional spatial patterns of XCO₂ compared to origin carbon satellite monitoring and previous XCO₂ products. The global pattern of XCO₂ exhibited a distinct increasing trend with a growth rate of 2.32 ppm yr⁻¹, reaching 414.00 ppm in 2021. Globally, XCO₂ showed obvious spatial variability across different latitudes and continents. Higher XCO₂ concentrations were primarily observed in the Northern Hemisphere, particularly in regions with intensive anthropogenic activity, such as East Asia and North America. We also validated the effectiveness of our XCO₂

products in detecting intensive CO₂ emission sources. The XCO₂ dataset is publicly accessible on the Zenodo platform at https://doi.org/10.5281/zenodo.12706142 (Wang et al., 2024a). Our products enable enhanced ability in identifying regional- and county-level XCO₂ hotpots, carbon emissions and fragmented carbon sinks, providing a robust basis for targeted global carbon governance policies.

1 Introduction

Carbon dioxide (CO₂) is a primary greenhouse gas (GHG). Anthropogenic activities and land use change since the industrial revolution have led to a marked increase in atmospheric CO₂, which is widely considered to be a major contributor to climate change, reaching a record-high of 414.71 parts per million (ppm) in 2021 (Friedlingstein et al., 2022). The damaging global climate change caused by atmospheric increases in CO₂ is severe and irreversible (IPCC, 2023; Kemp et al., 2022; Solomon et al., 2009). Consequently, the Paris Agreement announced to hold "the increase in the global average temperature to well below 2 °C above preindustrial levels" and pursue efforts "to limit the temperature increase to 1.5 °C above pre-industrial levels". It was also determined that the joined parties should submit their nationally determined contributions (NDCs) to reduce CO₂ emissions.

Accurate monitoring of atmospheric CO₂ concentrations is crucial for measuring global CO₂ emissions mitigation as well as characterizing terrestrial carbon change. Currently, ground-based and airborne platform-based atmospheric CO₂ observation networks, such as the Total Carbon Column Observing Network (TCCON, https://tccondata.org/, last access: 11 September 2025), are capable of providing CO₂ measurements with high accuracy (Petzold et al., 2016; Wunch et al., 2011, 2010). However, these observation networks are insufficient to fully explore the spatiotemporal patterns of atmospheric CO₂ at a global scale. The launch of a series of carbon observation satellites in recent years has provided favorable opportunities for continuous and largescale atmospheric CO₂ observation (Buchwitz et al., 2015; Hammerling et al., 2012). The Scanning Imaging Absorption Spectrometer for Atmospheric Chartography (SCIA-MACHY) onboard EnviSat was one of the first instruments to monitor the atmospheric column-averaged dry-air mole fraction of CO₂ (XCO₂) (Bovensmann et al., 1999). The Greenhouse Gases Observing Satellite (GOSAT) launched by Japan utilized the Thermal And Near-Infrared Sensor for carbon Observation (TANSO) instrument to monitor XCO2 globally, providing products with a spatial resolution of 10 km every three days (Butz et al., 2011). The Orbiting Carbon Observatory-2 (OCO-2) and OCO-3 launched by NASA provide XCO₂ measurements at a finer spatial resolution (Eldering et al., 2017). These sensors are considered among the best for XCO₂ observation, featuring larger overlapping swaths that cover areas of $\sim 20 \times 80 \,\mathrm{km^2}$ and exhibiting the

least retrieval absolute bias, measuring less than 0.4 ppm (Eldering et al., 2019; Taylor et al., 2020). However, the narrow swath of the sensor can only cover limited spatial areas, and caused by the cloud and aerosol contaminations, the data from OCO-2/3 always contain large amount of missing values (Taylor et al., 2016; Crisp et al., 2017). These limitations obstacle the better understanding of the atmosphere-land carbon cycle over large spatial scale based on satellite observation.

Consequently, several studies have concentrated on generating spatially continuous XCO₂ products based on satellite observations (He et al., 2022; Siabi et al., 2019; Zhang and Liu, 2023). One potential solution is the application of diverse interpolation methods (He et al., 2020; Zeng et al., 2014). However, their results encounter large uncertainty in regions with sparse data coverage, due to the coarse spatial resolution of the original data. In addition, data fusion techniques have gained recognition as an effective method for obtaining full-coverage XCO2 data (Sheng et al., 2022; He et al., 2022; Siabi et al., 2019; Zhang and Liu, 2023). These techniques can be broadly categorized into two groups. The first category leverages the spatiotemporal correlation inherent in multi-source XCO₂ data, fusing them based on this spatiotemporal information (Wang et al., 2023; Sheng et al., 2022). For instance, Wang et al. (2023) introduced a spatiotemporal self-supervised fusion model and generate seamless global XCO₂ data at a spatial resolution of 0.25°. The second category is regression-based methods, which aim to fill the gap by capturing the nonlinear relationship between multi-source XCO₂ measurements and related covariates (He et al., 2022; Siabi et al., 2019; Zhang and Liu, 2023). The specific methodologies include traditional statistical models, geostatistical models and machine learning models. Siabi et al. (2019) employed the Artificial Neural Network (ANN) to establish correlation between XCO₂ and eight environmental variables. Zhang and Liu (2023) utilized the convolution neural networks (CNN) coupled with attention mechanisms to produce full-coverage XCO2 data across China. Recently, Zhang et al. (2023) developed high spatial resolution global CO₂ concentration data based on deep forest model and multi-source satellite products.

Although the development of CO₂ observation satellites and the application of machine learning methods have significantly improved the estimation accuracy of XCO₂, current studies still face several limitations. Firstly, due to the sparse distribution of satellite XCO₂ data, previous studies always relied on assimilation and reanalysis XCO₂ data, such

as CAMS XCO₂ with coarse spatial resolution (0.75°). This reliance often results in final products that closely mirror the assimilation and reanalysis results, leading to an oversmoothed distribution that undermines the high-resolution advantages of satellite data. Furthermore, most current studies estimated the spatial distribution of CO₂ primarily based on vegetation and meteorological information, with limited consideration of the impact of human activities and emissions, despite these have significant influence on atmospheric CO₂ variability. This limitation also led to estimation results that fail to adequately capture the impact of anthropogenic emissions on atmospheric CO₂. In addition, most studies that employ regression models to estimate full-coverage XCO₂ are limited to regional or national scales due to the weak transferability of these models (Chen et al., 2022). Only a few studies (Zhang et al., 2023) have explored global-scale CO₂ estimation using machine learning approaches, highlighting the need for further research to enhance model generalizability and scalability. Therefore, we intent to develop the global full-coverage XCO₂ products with the capacity to capture both large-scale patterns and fine spatial details. This development leveraged satellite carbon monitoring, multisource high spatial resolution auxiliary variables and advanced methods that exhibit spatiotemporal transferability to overcome the aforementioned limitations.

In this study, we leveraged time-series OCO-2/3 XCO₂ data and various related environmental variables from multisource satellites to generate global full-coverage XCO₂ products. The advanced deep learning method was adopted to model time-series XCO₂ and incorporate terrestrial flux, anthropogenic flux and climatic impacts into the parameterization process. These products are designed to meet the following criteria: (1) high validated accuracy to ensure the reliability of the estimates, (2) high spatial resolution capable of capturing fine-scale variations in CO₂ concentrations, and (3) global full-coverage that overcomes missing values in satellite carbon observations. Our XCO₂ products achieved full global coverage with a spatial resolution of 0.05° and a monthly temporal resolution from 2015 to 2021. We also validated our XCO₂ products against in-situ XCO₂ data and other XCO2 products. Based on our high-resolution products, we explored the spatial and temporal pattern of atmospheric CO₂ globally and identified regions with intense CO₂ emission. Our findings aim to enhance the understanding of carbon dynamics on a global scale through data reconstruction and analysis.

2 Materials and methods

In this study, we utilized Google Earth Engine (GEE) to integrate OCO-2/3 XCO₂ data and multiple environmental variables as data inputs. In addition, the attention-based Bidirectional Long Short-Term Memory (At-BiLSTM) model was trained for building the relationship between OCO-2/3 XCO₂

and the related environmental variables. Then, we reconstructed the global monthly XCO_2 and validated the accuracy of the products against $TCCON\ XCO_2$ data and the original $OCO-2/3\ XCO_2$ data. We also analyzed the spatial and temporal variation of XCO_2 over the globe and detect the intense CO_2 emission regions. The methodology framework is shown in Fig. 1.

2.1 Datasets

2.1.1 OCO XCO2 data

In this study, we utilized the satellite-based XCO2 data from OCO-2 and OCO-3, covering the period from December 2014 to December 2021. The OCO-2/3 measure at three near-infrared wavelength bands, that are 0.76 µm Oxygen Aband, 1.61 µm weak CO₂, and 2.06 µm strong CO₂ bands (Crisp et al., 2004). The full physics retrieval algorithm was used to retrieve the XCO₂ based on the observation of the two satellites (Crisp et al., 2021). Previous studies (Taylor et al., 2023) suggested that the OCO-2 and OCO-3 XCO₂ measurements are in broad consistency and can therefore be used together in scientific analyses. The OCO-3 Level 2 XCO₂ Lite version 10.4r data (OCO₃ L₂ Lite FP V10.4r) (OCO-2/OCO-3 Science Team, 2022) from 2020 to 2021 and the OCO-2 Level 2 XCO₂ Lite version 11r (OCO2_L2_Lite_FP V11r) (OCO-2 Science Team, 2020) from 2015 to 2019 were downloaded from Goddard Earth Sciences Data and Information Services Center (GES DISC, https://disc.gsfc.nasa.gov/, last access: 11 September 2025). The products were aggregated as a daily file (Fig. 2) with a spatial resolution of $2.25 \,\mathrm{km} \times 1.29 \,\mathrm{km}$ (O'Dell et al., 2018). The XCO₂ data were quality filtered, and only goodquality data (i.e., xco2_quality_flag = 0) were considered. To generate the monthly products with a spatial resolution of $0.05^{\circ} \times 0.05^{\circ}$, we converted the daily data to monthly data by averaging the sparse XCO2 data within a range of $0.05^{\circ} \times 0.05^{\circ}$ over one month.

2.1.2 TCCON XCO2 data

The Total Carbon Column Observing Network (TCCON) is a global network for measuring atmospheric CO_2 , methane (CH₄), carbon monoxide (CO) and other trace gases in the atmosphere. The XCO_2 data from TCCON were demonstrated to have high accuracy with $\sim 0.2\,\%$ of XCO_2 (Wunch et al., 2011). Consequently, the data have been used widely for the validation of satellite observations such as OCO-2, OCO-3 and GOSAT (Deng et al., 2016; Wunch et al., 2017). In this research, we used the GGG2014 and GGG2020 datasets from 23 sites (Fig. 3 and Table 1) around the world to validate the reconstructed XCO_2 products.

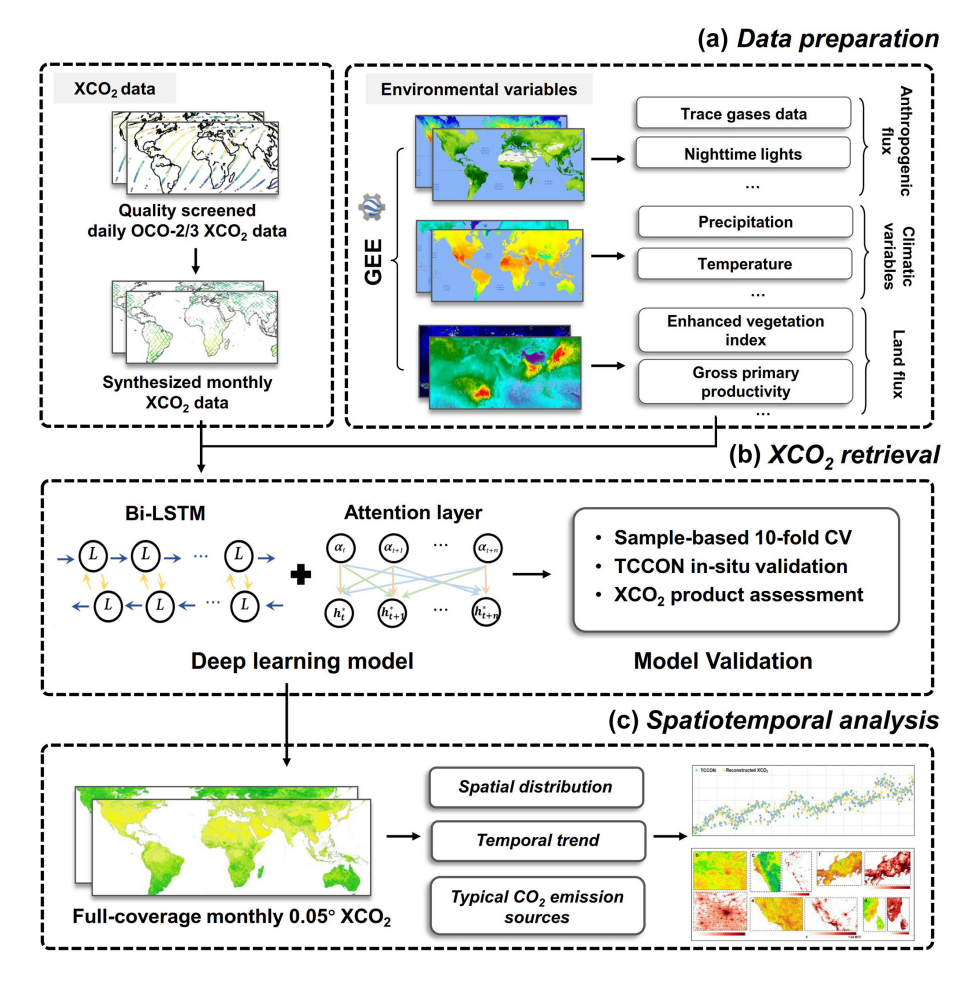


Figure 1. The workflow for mapping and exploring global XCO₂ dynamics and drivers.

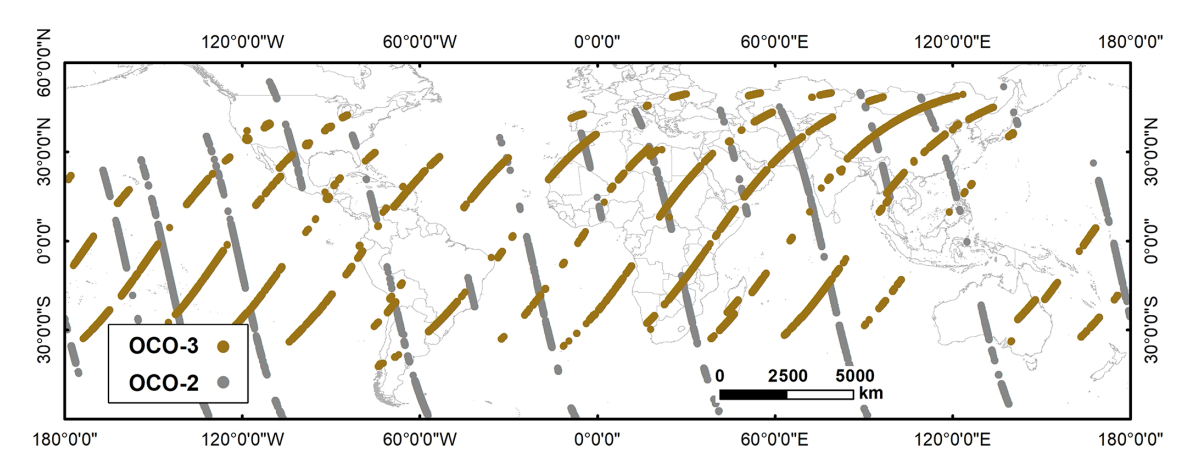


Figure 2. Footprints of OCO-2 and OCO-3 XCO₂ data on 20 January 2018 and 4 December 2021 (with quality filtering) as examples.

2.1.3 Environmental variables

In the selection of environmental variables, our primary focus was on processes within the terrestrial carbon cycle. The carbon cycle on land can be conceptualized as two flux exchange processes influenced by the climatic conditions (Fig. 4). The CO₂ in the atmosphere is fixed by vegetation photosynthesis and the carbon is released back into the atmosphere by respiration and disturbance processes (Beer et al., 2010; Pan et al., 2011). The carbon fluxes through these processes we considered as the land flux. Since Industrial

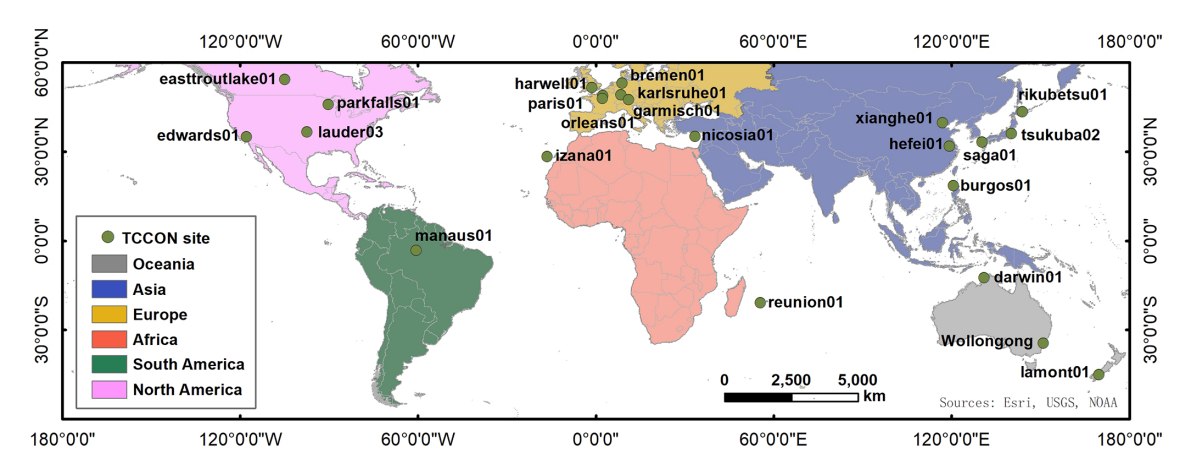


Figure 3. The locations of the TCCON sites.

Table 1. The information on the TCCON *in situ* stations.

ID	Site name	Longitude	Latitude	Start date	End date (yyyy/mm/dd)
1	saga01 (JP)	130.29	33.24	2011/07/28	2021/06/30
2	xianghe01 (PRC)	116.96	39.80	2018/06/14	2022/04/09
3	burgos01 (PH)	120.65	18.53	2017/03/03	2021/08/20
4	harwell01 (UK)	-1.32	51.57	2021/05/30	2022/05/22
5	bremen01 (DE)	8.85	53.10	2009/01/06	2021/06/24
6	tsukuba02 (JP)	140.12	36.05	2014/03/28	2021/03/31
7	lauder03 (NZ)	-97.49	36.60	2018/10/02	2022/11/14
8	edwards01 (US)	-117.88	34.96	2013/07/20	2022/12/25
9	nicosia01 (CY)	33.38	35.14	2019/09/06	2021/06/01
10	izana01 (ES)	-16.5	28.31	2014/01/02	2022/10/31
11	orleans01 (FR)	2.11	47.96	2009/09/06	2022/04/24
12	hefei01 (PRC)	119.17	31.90	2015/11/02	2020/12/31
13	easttroutlake01 (CA)	-104.99	54.35	2016/10/03	2022/08/13
14	karlsruhe01 (DE)	8.44	49.10	2014/01/15	2023/01/20
15	paris01 (FR)	2.36	48.85	2014/09/23	2022/03/28
16	garmisch01 (DE)	11.06	47.48	2007/07/18	2021/10/18
17	rikubetsu01 (JP)	143.77	43.46	2014/06/24	2021/06/30
18	lamont01 (US)	169.68	-45.04	2011/04/16	2022/12/19
19	reunion01 (RE)	55.48	-20.90	2015/03/01	2020/07/18
20	darwin01 (AU)	130.93	-12.46	2005/08/28	2020/04/30
21	Wollongong (AU)	150.88	-34.41	2008/06/26	2020/06/30
22	Manaus01(BR)	-60.60	-3.21	2014/09/30	2015/07/27
23	parkfalls01 (US)	-90.27	45.94	2004/06/02	2020/12/29

JP: Japan, DE: Germany, FI: Finland, FR: French, RE: Réunion Island, AU: Australia, BR: Brazil; US: United States, PRC: People's Republic of China, NO: Norway, CY: Cyprus, NZ: New Zealand, PH: Philippines, UK: United Kingdom, CA:

Era, anthropogenic carbon from land use change (e.g., deforestation) and fossil fuels and cement become important parts of atmospheric CO₂ (Friedlingstein et al., 2010), which we considered as the anthropogenic flux. Meanwhile, the two processes are directly or indirectly driven by the climatic features (Sitch et al., 2015; Chen et al., 2021). Consequently, we explored the potential drivers of XCO₂ from the perspective of the carbon cycle at atmosphere-land interface. Multiple satellite products and reanalysis data from three aspects (i.e.,

land flux, anthropogenic flux and climatic impacts) were selected to consider their various effects on the XCO₂.

The key factors selected related to the land flux included gross primary productivity (GPP), enhanced vegetation index (EVI), land surface temperature (LST), vegetation continuous fields (VCF), and normalized difference snow index (NDSI). These products are all obtained from the Moderate Resolution Imaging Spectroradiometer (MODIS), which has been operated for over 20 years and produced various

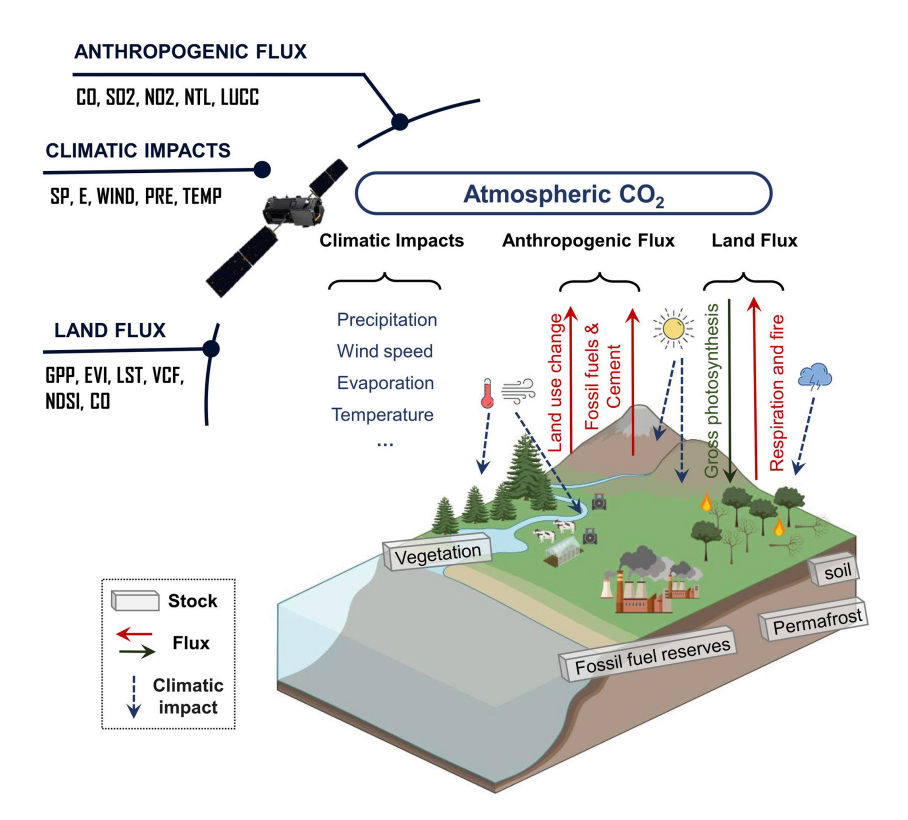


Figure 4. Simplified illustration of the global carbon cycle on land (referring to IPCC, 2023). Noting that the carbon cycle in the ocean was not considered in our study and we only focused on the fast exchange fluxes. The slow carbon exchanges (e.g., chemical weathering, volcanic emissions) which are generally assumed as relatively constant over the last few centuries (Sundquist, 1986), were not included here.

satellite products with fine spatial resolution and accuracy. The EVI and NDSI were converted to monthly data using the maximum value composite (MVC) method. The GPP and LST were converted to monthly data by the averaging method.

The rising anthropogenic activities have greatly influenced atmospheric CO₂ (Friedlingstein et al., 2022). In this study, five anthropogenic factors, including land use/cover change (LUCC), nighttime lights (NTL), and three trace gases (i.e., sulfur dioxide (SO₂), nitrogen dioxide (NO₂), and carbon monoxide (CO)) were selected. The LUCC was obtained from MODIS MCD12Q1 with a spatial resolution of 500 m. The monthly Suomi National Polar-orbiting Partnership-Visible Infrared Imaging Radiometer Suite (NPP-VIIRS) day/night band (DNB) NTL products (spatial resolution of 15 arcsec, \sim 500 m) were obtained from the Earth Observation Group (EOG) of the Colorado School of Mines. We also used the SO₂, NO₂ and CO products from the TROPOspheric Monitoring Instrument (TROPOMI) onboard Sentinel-5 Precursor (S5P), a global air monitoring satellite for the Copernicus mission. The data were also converted to the same temporal resolution (i.e., monthly).

The selected climatic factors affecting XCO_2 were surface pressure (SP), 10 m wind speed (WS), precipitation flux (PRE), 2 m air temperature (Temp), and total evaporation

(E). These data are from the reanalysis products (Hersbach et al., 2020) developed at the European Center for Medium Weather Forecasting (ECMWF, https://www.ecmwf.int/, last access: 11 September 2025). The WS is calculated using the products of 10 m wind components of U and V. All data were converted to monthly time-series. The bilinear interpolation approach was employed both to fill gaps in the ancillary data and to convert the data at different spatial resolutions to 0.05° resolution. The data preprocessing was conducted on GEE, R and ArcGIS 10.3. Details of these products are listed in Table 2.

2.2 Deep learning-based XCO₂ reconstruction

Given the complexity temporal dependence and nonlinear relationship between XCO₂ and the environmental variables, we selected the At-BiLSTM model to relate the XCO₂ data with the 16 response variables affecting atmospheric CO₂, and further reconstruct the XCO₂ data at a fine spatial resolution. The LSTM model is a variant of RNN that excels in modeling temporal sequences and capture long-range dependencies (Hochreiter and Schmidhuber, 1997; Graves and Schmidhuber, 2005), which is essential for understanding the seasonal variations of XCO₂ and dynamic feedbacks between XCO₂ and environmental drivers we selected. Each

Variables Spatial resolution Temporal resolution Product names Category **GPP** 500 m 8 d MOD17A2H Land flux-related **EVI** 16 d 1 km MOD13A2 LST 1 km daily MOD11A1 VCF 250 m annual MOD44B **NDSI** $500 \, \text{m}$ MOD10A1 daily LUCC $500 \, \text{m}$ annual MCD12Q1 Anthropogenic flux-related NTL VNP46A2 15 arcsec monthly SO_2 $\sim 1 \text{ km}$ OFFL/L3_SO₂ daily NO_2 OFFL/L3_NO₂ CO OFFL/L3_CO SP $\sim 10 \,\mathrm{km}$ monthly ERA5-Land Climatic impacts Е Wind-vWind-u Pre Temp

Table 2. Ancillary variables selected in this study.

LSTM cell includes an input gate, a forget gate and an output gate. The forget gate f_t determines which information from the previous time step to forget (Eq. 1):

$$f_t = \sigma(\mathbf{W}_{\mathbf{f}} \cdot \left[\mathbf{h}_{t-1}, \mathbf{x}_t \right] + \mathbf{b}_{\mathbf{f}}) \tag{1}$$

where σ , \mathbf{W}_f , $[\mathbf{h}_{t-1}, \mathbf{x}_t]$, and \mathbf{b}_f denotes the sigmoid activation function, vectors of weights, concatenation of the hidden state at timestep t-1 and the current input, and the bias vector, respectively.

The input gate i_t governs the selective storage of the data in current time step, and the output from forget gate f_t and input gate i_t are combined in the cell state C_t (Eqs. 2–3):

$$\mathbf{i}_{t} = \sigma \left(\mathbf{W}_{i} \cdot \left[\mathbf{h}_{t-1}, \mathbf{x}_{t} \right] + \mathbf{b}_{i} \right) \tag{2}$$

$$C_t = f_t \cdot C_{t-1} + i_t \cdot \tanh\left(\mathbf{W}_c \cdot \left[\mathbf{h}_{t-1}, \mathbf{x}_t\right] + \mathbf{b}_c\right)$$
(3)

where \mathbf{W}_i and \mathbf{W}_c denote the weight matrix for the input gate and the current cell state, respectively; \mathbf{b}_i and \mathbf{b}_c are the bias vector of the input gate and the current cell state, respectively; \mathbf{C}_{t-1} and tanh represent the cell state at timestep t-1 and the activation function.

Lastly, the output gate o_t controls the flow of information from the cell state to the next time step (Eq. 4).

$$\mathbf{o}_t = \sigma(\mathbf{W}_0 \cdot \left[\mathbf{h}_{t-1}, \mathbf{x}_t \right] + \mathbf{b}_0) \tag{4}$$

where W_0 and b_0 denotes the weight matrix and the bias vector of the output gate, respectively.

These gate structures effectively manage the flow of information within the LSTM, enabling it to capture the temporal dependencies present in the data (Yuan et al., 2020; Wang et al., 2022). Bidirectional LSTM consists of two directional LSTM, in which the data flows forward and backward (Graves et al., 2013). The bidirectional structure was chosen to enhance the capability of LSTM by allowing the

model to consider both past and future context in the time series, thereby providing a more comprehensive understanding of the underlying temporal dynamics.

We also defined a multi-dimensional attention layer behind the BiLSTM to focus on more critical timesteps and give them higher weights (Bahdanau et al., 2016). This is particularly important when dealing with high-dimensional input data comprising multi-timestep variables, as it allows the model to assign different weights to different timesteps, thereby improving interpretability and predictive performance (Liu and Guo, 2019; Wang et al., 2024b). Based on this framework, the At-BiLSTM model offers a robust and flexible framework for linking XCO₂ with multiple environmental variables and reconstructing XCO₂ at a fine spatial resolution with improved accuracy and spatiotemporal consistency.

The At-BiLSTM consists of one input layer, three Bidirectional LSTM (Bi-LSTM) layers, one attention layer, one dropout layer to prevent overfitting, and one fully connected layer (i.e., dense layer) for the final output. Each Bi-LSTM includes 512 hidden units and tanh activation in both forward and backward directions. The attention mechanism learns a weight distribution over the time dimension using a Dense layer with softmax activation, then multiplies these weights with the BiLSTM output to emphasize important time steps. The detailed deployment and output are provided in Table 3. The model was implemented using the TensorFlow and Keras deep learning APIs in Python. A time step of 3 was used, and the model was trained for 200 epochs with the mean squared error (MSE) as the loss function. A stepwise decay strategy was applied to the learning rate, where the rate was reduced by a factor of 10 every 50 epochs to enhance training stability and convergence. Prior to training,

all input data were normalized using the mean and standard deviation of the dataset.

In this study, we adopted the sample-based cross-validation (CV) method to evaluate the model performance and the in-situ validation to assess the accuracy of reconstructed XCO₂ products. We also compared the reconstructed XCO₂ products with the original OCO XCO₂ products and the CAMS-EGG4 GHGs data. Four metrics, including coefficient of determination (R^2), root mean squared error (RMSE), mean absolute error (MAE) and mean bias, were calculated as follow, to assess the model performance.

$$R^{2} = 1 - \frac{\sum_{i=1}^{n} (y_{i} - f_{i})^{2}}{\sum_{i=1}^{n} (y_{i} - \overline{y})^{2}}$$
 (5)

RMSE =
$$\sqrt{\frac{\sum_{i=1}^{n} (y_i - f_i)^2}{n}}$$
 (6)

$$MAE = \frac{\sum_{i=1}^{n} |(f_i - y_i)|}{n}$$
 (7)

where n is the total number of data samples, and f_i , y_i are the observed results and model-estimated results, respectively.

3 Results

3.1 Validation of the reconstructed XCO₂ product

3.1.1 Model validation results

Given the distinct seasonal variation in XCO_2 concentrations, we conducted the sample-based CV to evaluate the model performance during different seasons (Fig. 5). The model demonstrated high accuracy across all seasons, with R^2 values exceeding 0.81, MAE less than 0.73 ppm, and RMSE less than 1.09 ppm. The model performed better in spring and summer, as indicated by the densest cluster of points being closest to the 1:1 line. Conversely, the model performed worst in winter, when photosynthesis is weakest, leading to greater estimation deviation. These variations are likely influenced by the ecosystem CO_2 exchange during different seasons. Overall, the model effectively captured the seasonal variation of XCO_2 and provided unbiased XCO_2 estimations.

We further validated the model performance across different continents. Table 4 presents the validation results for six continents. The model performance varied across continents. Notably, the model achieved the highest accuracy in Africa and Europe, with R^2 of 0.80 and 0.81, and RMSE values of 1.02 and 1.14 ppm, respectively. In contrast, the model demonstrated relatively low accuracy in Oceania and South America, both located in the southern hemisphere. Despite this, the RMSE of the model in these continents were 1.22 and 0.66 ppm, respectively, indicating that the model maintained acceptable estimation accuracy in these regions.

3.1.2 In situ validation results

The TCCON in situ XCO₂ data were adopted for validating the accuracy of the reconstructed XCO₂ over the globe. The validation results for our reconstructed XCO2 and the origin OCO-2/3 XCO₂ are displayed in Fig. 6. The two XCO₂ data showed similar precision with the R^2 value of 0.91 and 0.92, respectively (Fig. 6c-d). While the reconstructed XCO₂ greatly increases the data coverage with the validation sample increasing from 578 to 1432. Meanwhile, the reconstructed XCO2 has a smaller RMSE and MAE with values of 1.58 and 1.22 ppm, respectively, compared with the OCO XCO₂. These results indicate that the reconstructed XCO₂ had a closer agreement with TCCON XCO₂. We also displayed the mean bias of OCO and reconstructed XCO₂ in each TCCON site (Fig. 6a-b). As shown in Fig. 6a, the OCO-2/3 observation tend to overestimate the XCO₂, while the reconstructed XCO₂ could amend the underestimation of OCO XCO₂. Over 68 % of the validation sites of reconstructed XCO₂ had a mean bias less between ± 0.4 ppm. Given the orbital constraints of the ISS (Eldering et al., 2019), OCO-3 measurements were restricted to latitudes below $\pm 52^{\circ}$. Consequently, substantial missing values of OCO XCO₂ data were shown around 50° N, introducing a potential bias. In contrast, the reconstructed XCO₂ effectively solves this problem and demonstrates markedly enhanced performance.

Figure 7 shows the individual in situ validation results of the reconstructed XCO₂ against TCCON site in different continents (except Antarctica). The sample numbers are varying in different sites due to the observation constraints, while the validation results from all sites showed satisfying performance. The R^2 for all sites are over 0.88 and the MAE are less than 1.46 ppm. The reconstructed XCO₂ data performs the best in sites lauder03 and karlsruhe01, which located in North America and Europe, respectively. While the reconstructed XCO₂ performed worst in saga01 which located in Asia, potentially due to the high CO₂ concentrations in these regions. Overall, the reconstructed XCO₂ showed high consistency with the in situ XCO₂ observation in different regions over the globe.

To assess the performance of our reconstructed XCO₂ in temporal analysis, we compared the time series for monthly OCO-2/3, reconstructed and TCCON XCO₂ data from December 2014 to December 2021. As depicted in Fig. 8, the reconstructed XCO₂ exhibits similar temporal patterns compared to the TCCON data, with the mean RMSE and MAE of 1.47 and 1.07 ppm. While the OCO-2/3 XCO₂ exhibits some overestimation for high values and underestimation for low values compared with TCCON data. In contrast, the reconstructed XCO₂ provided more stable estimate results.

Table 3. Architecture of the At-BiLSTM model.

Layer Name	Layer	Parameters	Output size
Bi-LSTM	Input layer Bi-LSTM1 Bi-LSTM2 Bi-LSTM3	units = 512, activation = "tanh" units = 512, activation = "tanh" units = 512, activation = "tanh"	3×16 3×1024 3×1024 3×1024
Attention	Permute Dense Permute Multiply	units = 3, activation = "softmax" -	1024×3 1024×3 3×1024 3×1024
Dropout		rate = 0.5	
Full-connect	Dense	units = 1	1

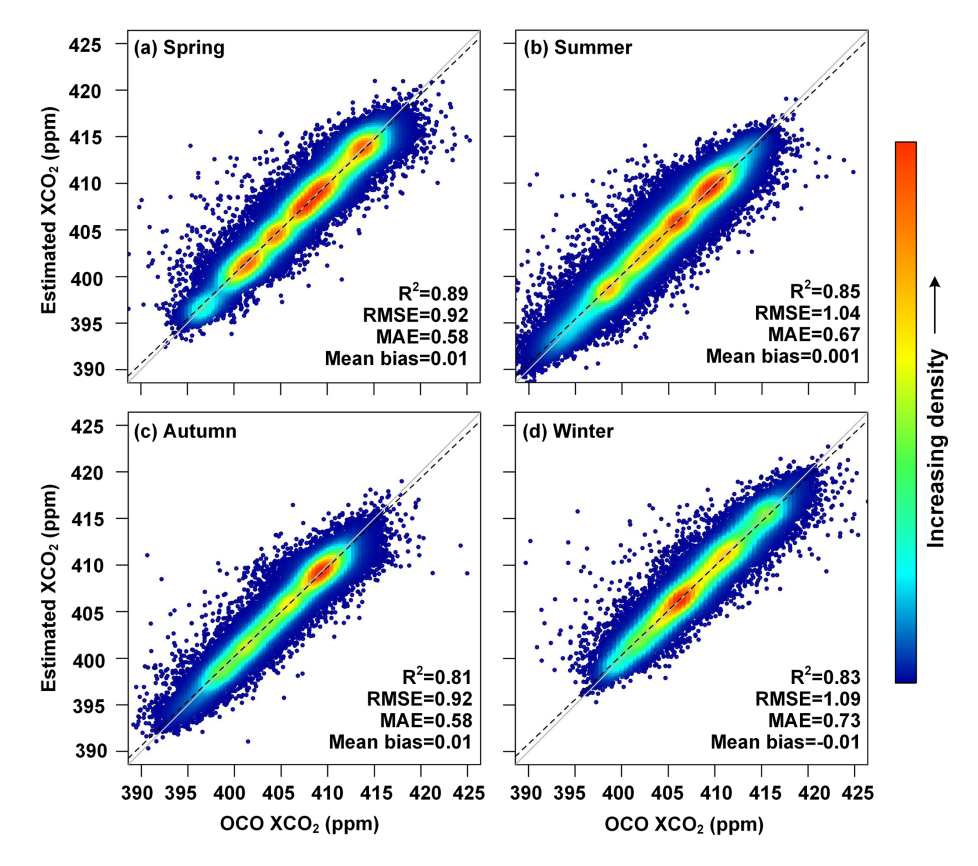


Figure 5. Density scatterplots of sample-based CV results during different seasons. The proportion of the number of points is represented as the color of the points. The black dashed lines and grey solid lines denote the linear regression fitted lines and the 1:1 line, respectively. The R^2 , RMSE (ppm), MAE (ppm), and mean bias (ppm) are provided.

3.2 Spatiotemporal pattern of global XCO₂

The global distribution of annual mean XCO₂ concentration from 2015 to 2021 is illustrated in Fig. 9. The results reveal pronounced spatial heterogeneity in XCO₂ concentrations, characterized by a marked hemispheric asymmetry. Specifically, the Northern Hemisphere exhibited systematically elevated XCO₂ levels compared to the Southern Hemisphere

sphere, consistent with latitudinal gradients driven by anthropogenic emission patterns and atmospheric transport dynamics. Regionally, North America, East Asia, Central Africa, and northwest of Southern America were identified as persistent hotspots of enhanced XCO₂. The high concentrations of XCO₂ in North America and East Asia stem primarily from the fossil fuel emission from energy production and transportation sectors. Whereas the tropical regions (i.e., Cen-

Table 4. Model performance in different continents.

	R^2	RMSE (ppm)	MAE (ppm)	Mean bias (ppm)
Africa	0.80	1.02	0.70	-0.009
Asia	0.73	1.27	0.85	0.002
Europe	0.81	1.14	0.77	-0.030
North America	0.73	1.26	0.83	-0.020
South America	0.59	1.22	0.86	-0.012
Oceania	0.67	0.66	0.4	0.051

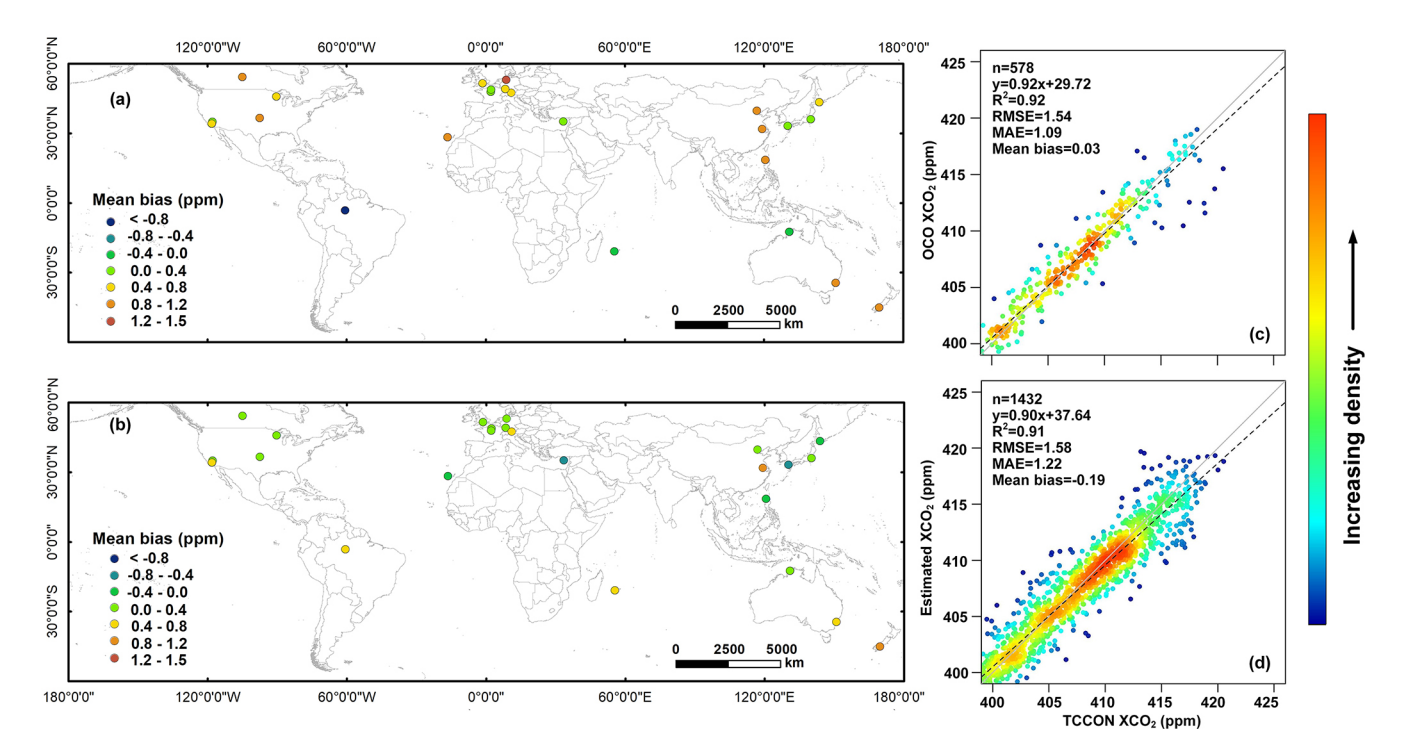


Figure 6. The mean bias of the (a) OCO observed XCO_2 , and (b) reconstructed XCO_2 against global TCCON XCO_2 ; (c) density scatterplots of the validation results for OCO observed XCO_2 , and (d) reconstructed XCO_2 against the TCCON XCO_2 . The proportion of the number of points is represented as the color of the points. The number of samples n, linear regression relation, R^2 , RMSE (ppm), MAE (ppm), and mean bias are provided.

tral Africa and South America) are influenced by coupled biomass burning and land-use changes.

We also provided the annual OCO-2 XCO₂ data from 2015 to 2019 and OCO-3 XCO₂ data from 2020 to 2021 in Fig. 10. Spatially, our reconstructed XCO2 dataset (Fig. 9) demonstrates robust consistency with satellite observations, particularly in mid-latitude industrialized regions where both datasets capture emission hotspots. Notably, OCO-3 exhibits denser observational sampling due to its improved spatial coverage and swath width compared to OCO-2's narrow tracks. However, persistent data gaps remain prevalent in both two satellite products after annual aggregating. These spatial coverage limitations hinder fine-scale global analysis, particularly in assessing localized emission sources and regional scale carbon flux.

Figure 11 presents the spatial distribution of the 7-year (2015-2021) averaged XCO₂ concentration and trend over the globe. The average XCO₂ concentration from 2015 to 2021 was 406.90 ± 0.80 ppm worldwide. The highest concentration of XCO2 mainly occurs in the northern low-tomid-latitudes (10-45° N). More frequent human activities and carbon emissions contributed to higher atmospheric CO2 concentrations in the Northern Hemisphere. In contrast, the lowest XCO₂ concentration was 404.02 ppm, occurring in the Southern Hemisphere where 81 % of the area is ocean. The oceans act as a vital carbon sink and absorb most atmospheric CO₂. For the continent scale, the XCO₂ concentrations showed a slight variation (±1 ppm) between different continents. The largest XCO2 were mainly occurred in Asia and North America over years, while the lowest XCO₂ concentration all presented in Oceania (Table 5). In terms

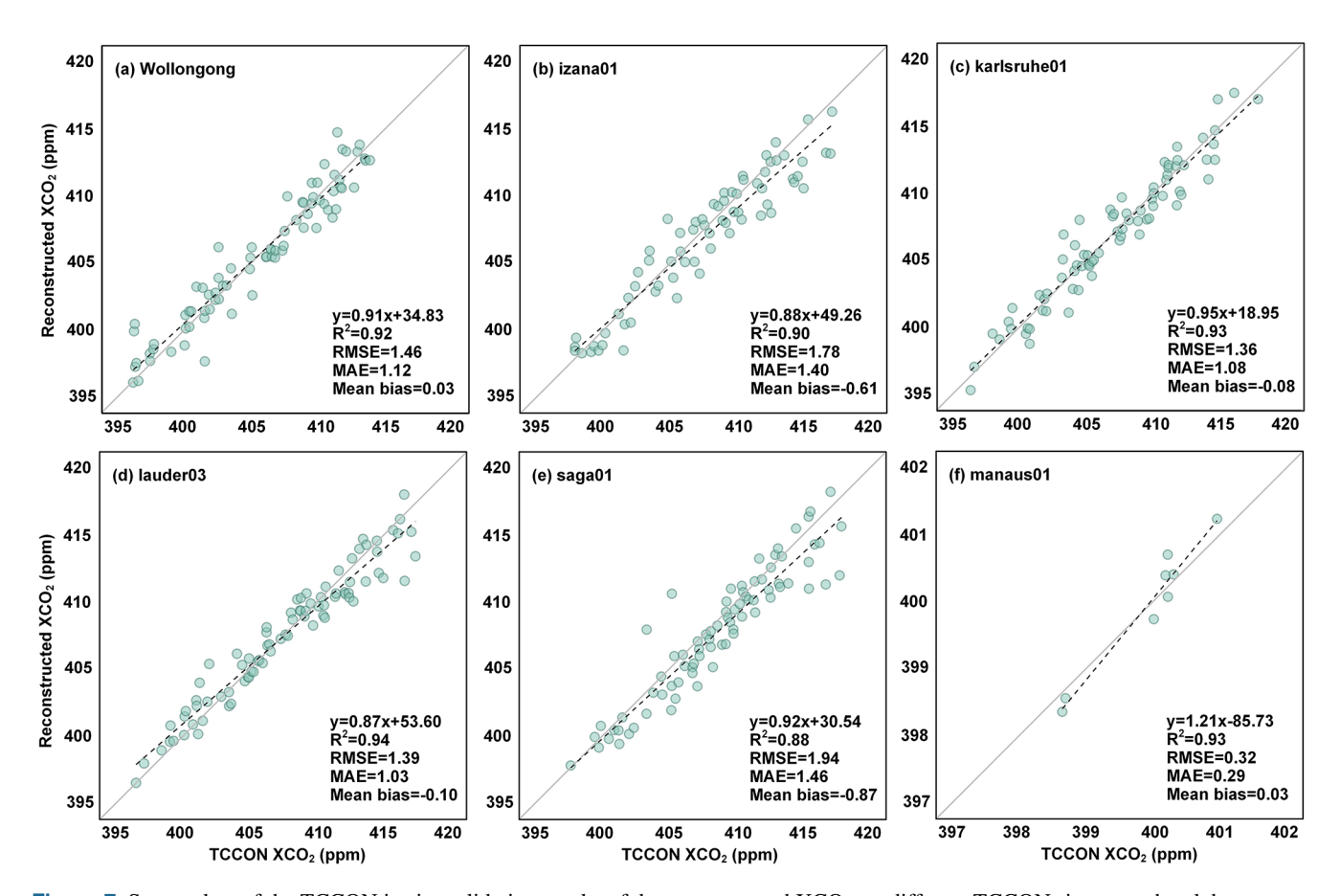


Figure 7. Scatterplots of the TCCON in situ validation results of the reconstructed XCO₂ on different TCCON sites over the globe.

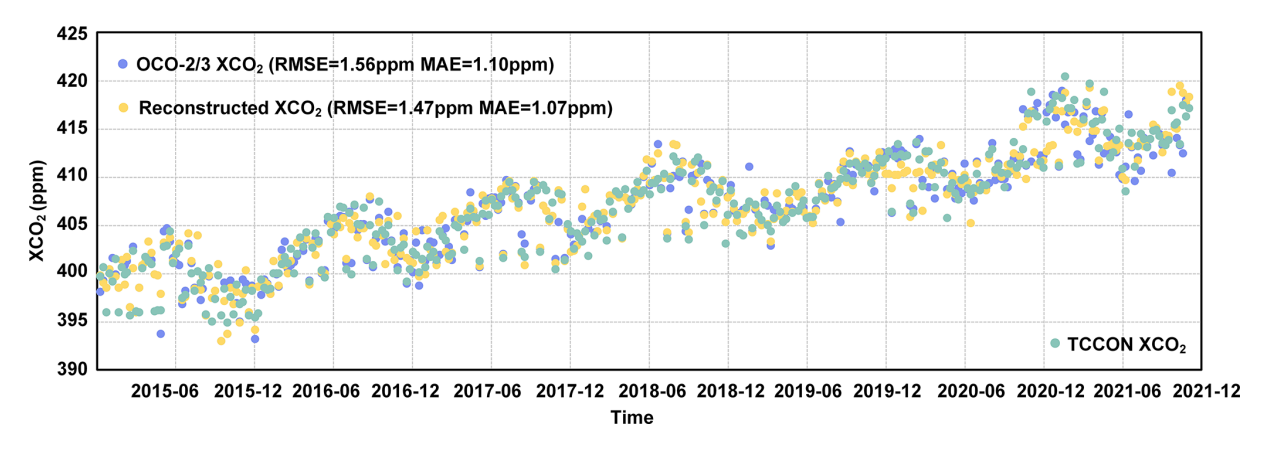


Figure 8. Comparison of the temporal variation of XCO₂ data from OCO-2/3 (blue dots), TCCON (green dots), and the reconstructed products (yellow dots).

of temporal trend, the atmospheric CO_2 exhibited a distinct increasing trend over time, with the mean growth rate of $2.32 \,\mathrm{ppm}\,\mathrm{yr}^{-1}$. The large growth rate meanly occurs in the northern low latitudes $(0-30^{\circ}\,\mathrm{N})$, especially the Middle East and North Africa (growth rate over $2.5 \,\mathrm{ppm}\,\mathrm{yr}^{-1}$). Globally, the XCO_2 increased by $14.16 \,\mathrm{ppm}$ over seven years (Table 4), especially in 2021, with increased values of up to

3 ppm. This result is consistent with the Global Carbon Budget 2022 (Friedlingstein et al., 2022), which reported that the global average atmospheric CO₂ increased sharply in 2021 and reached 414.71 ppm.

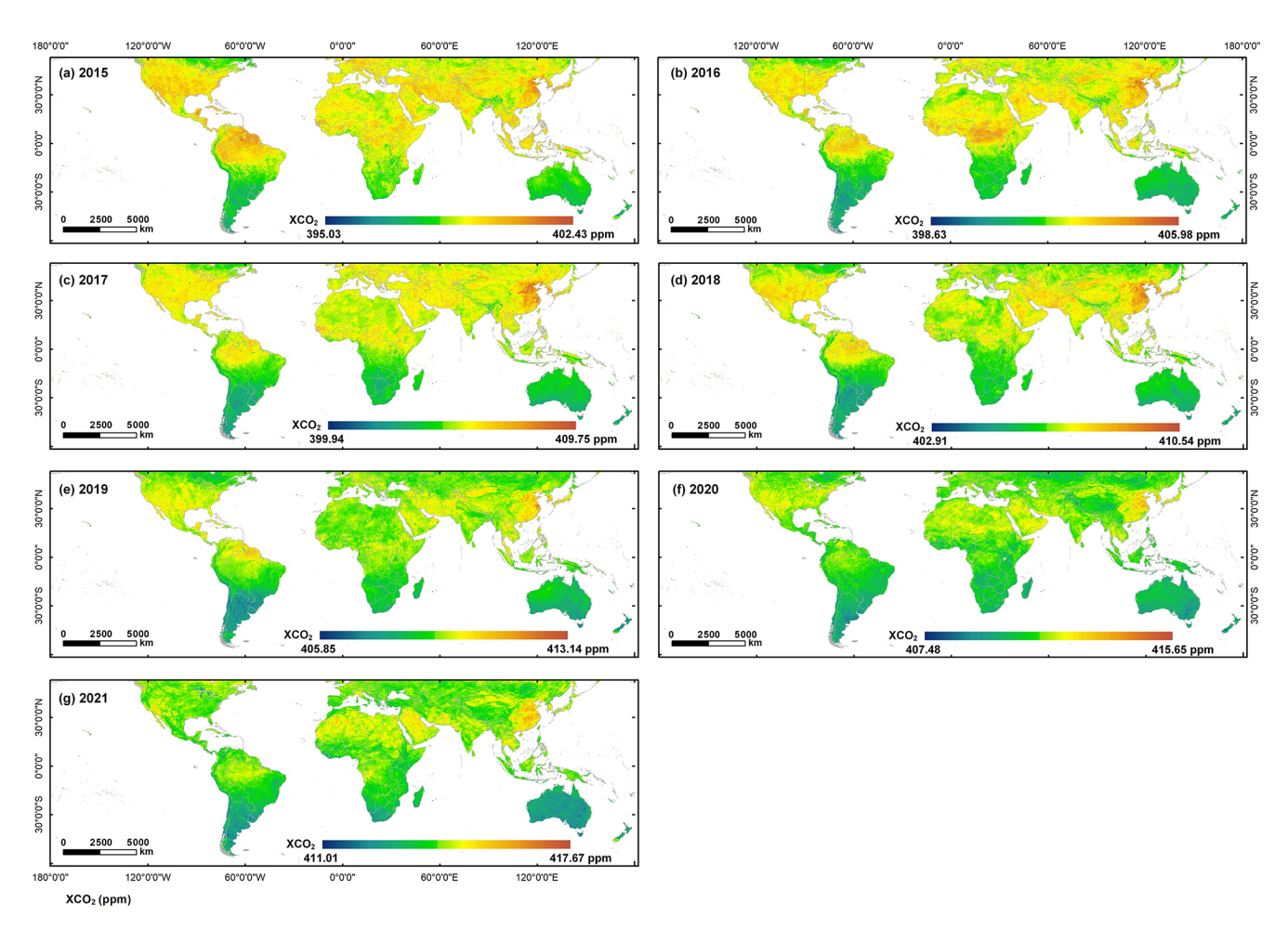


Figure 9. The global spatial distribution of reconstructed annual mean XCO₂ concentration from 2015 to 2021.

Table 5. The reconstructed XCO₂ concentrations at different continents from 2015 to 2021. Note that the bold font highlights the highest XCO₂ concentrations among different continents in each year.

Continents	XCO ₂ concentrations (ppm)							
	2015	2016	2017	2018	2019	2020	2021	Increase
Africa	399.26	402.66	404.98	406.71	409.26	411.13	414.11	14.85
Asia	399.57	403.03	405.80	407.37	409.68	411.39	414.38	14.81
Europe	399.55	402.88	405.77	406.96	409.48	411.30	414.17	14.62
North America	399.60	402.95	405.76	407.32	409.70	411.61	414.28	14.68
South America	398.94	401.96	404.27	406.17	408.78	410.47	413.57	14.63
Oceania	398.03	401.04	403.31	405.53	408.13	409.82	412.55	14.52
Global	399.84	401.56	405.16	407.50	409.21	411.07	414.00	14.16

3.3 The distribution of XCO₂ anomaly

To better explore the dynamics of global carbon change, we further calculated the $\rm XCO_2$ anomalies based on the full-coverage $\rm XCO_2$ products and presented their global distributions from 2015 to 2021 (Fig. 12). The $\rm XCO_2$ anomalies were calculated by the statistical filtering method, that is, subtracting the global median $\rm XCO_2$ value from the global $\rm XCO_2$

distribution (Hakkarainen et al., 2016). The spatial pattern of XCO₂ anomalies were relatively consistent over seven years with no significant variations. From the global perspective, high XCO₂ anomalies mainly occurred in the Northern Hemisphere. East Asia has the largest XCO₂ anomalies with values ranging from 2 to 3 ppm, such as the east part of China. The Middle East, North Africa and the southern part of Northern America also experienced high XCO₂ anoma-

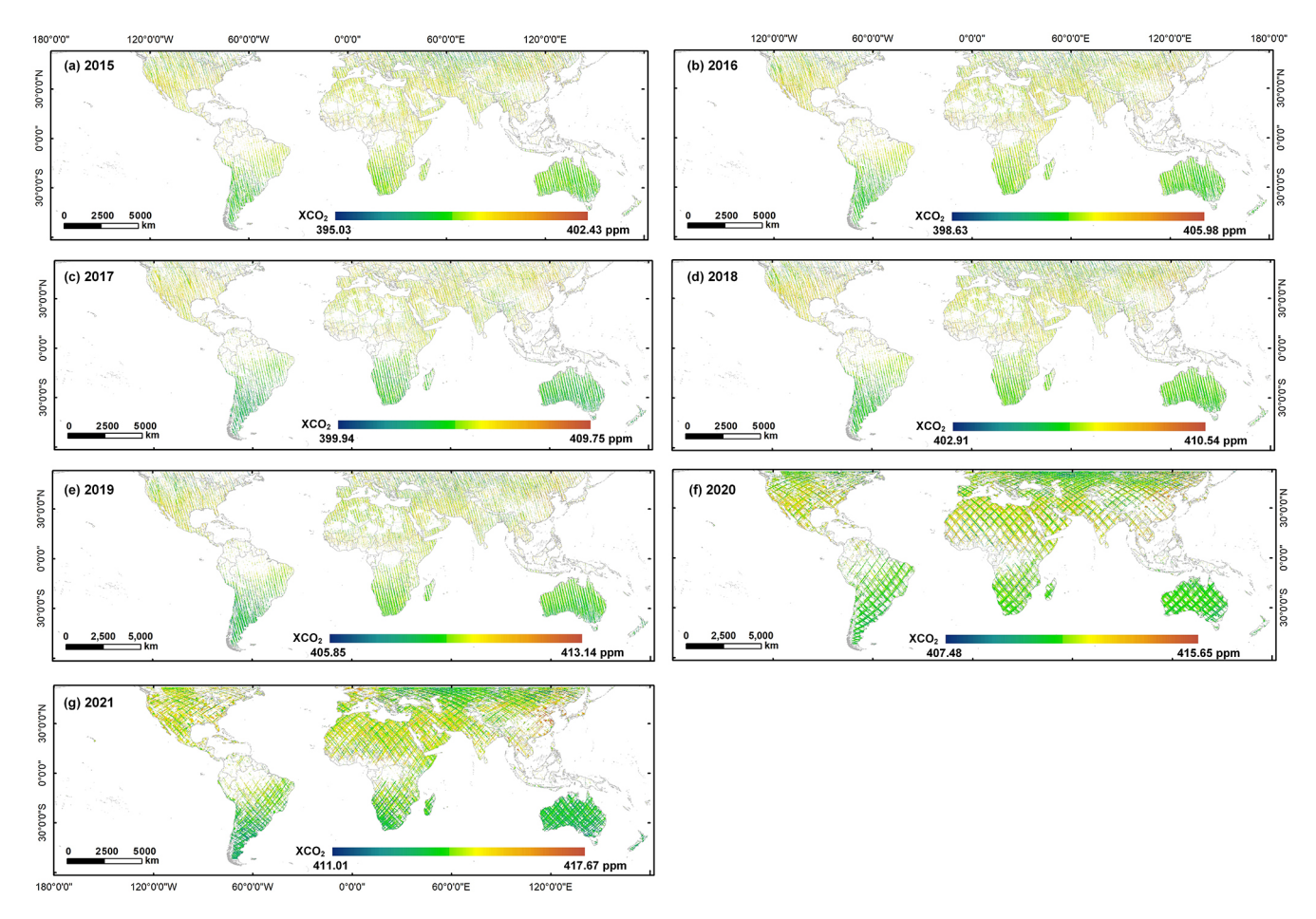


Figure 10. The global spatial distribution of annual mean OCO-2/OCO-3 XCO₂ concentration from 2015 to 2021.

lies. Nevertheless, negative XCO₂ anomalies were also identified in the Northern Hemisphere, specifically in regions such as Tibet in China, eastern Canada, and southern Russia. Most negative XCO₂ anomalies were observed in the Southern Hemisphere, which behaves as a carbon sink. However, some positive XCO₂ anomalies are also observed in the tropical regions (e.g., Amazonia), which indicates the Amazonia has changed into a carbon source due to the deforestation and fire occurrence in recent years (Hubau et al., 2020; Gatti et al., 2021).

Figure 13 illustrates the detailed spatial distribution of XCO₂ concentrations and anomalies over six regions with high XCO₂ retrievals in 2020. High concentrations of XCO₂ were typically associated with energy-intensive heavy industrial activities, such as Toa Oil Keihin Refinery Factory located in Kawasaki City, Japan (Fig. 13f), and the Shipping-port Industrial Park in Pennsylvania, United States (Fig. 13a). Moreover, certain metropolitan transport hubs also exhibited elevated CO₂ anomalies attributable to dense populations and intensive activities. Examples included Shanghai Station in China (Fig. 13e) and John F. Kennedy International Airport in New York, USA (Fig. 13b). Attention has

also been drawn to natural sources of emissions. Driven by the significant impact of agricultural mechanization and agro-industrial activities on cropland (Lin and Xu, 2018), the XCO₂ anomalies also occurred in the agricultural areas northwestern Jiangsu, China (Fig. 13d). Additionally, we also observed the high XCO₂ anomalies in Amazonia forest in Colombia, which have been suffered from deforestation (Gatti et al., 2023). In conclusion, our products could successfully capture the XCO₂ anomalies from different sources over the globe.

4 Discussion

4.1 Comparison with previous studies

To validate the effectiveness of our model and resulting XCO_2 products, we compared our results with current studies which focuses on global XCO_2 reconstruction (Table 6). As for the in-situ validation, most existing studies report high accuracy with almost all R^2 over 0.9, RMSE less than 2 ppm. Regarding spatial resolution, the various products differ substantially, ranging from 1° down to 0.01° . It should be noted that increasing spatial resolution tends to compromise the

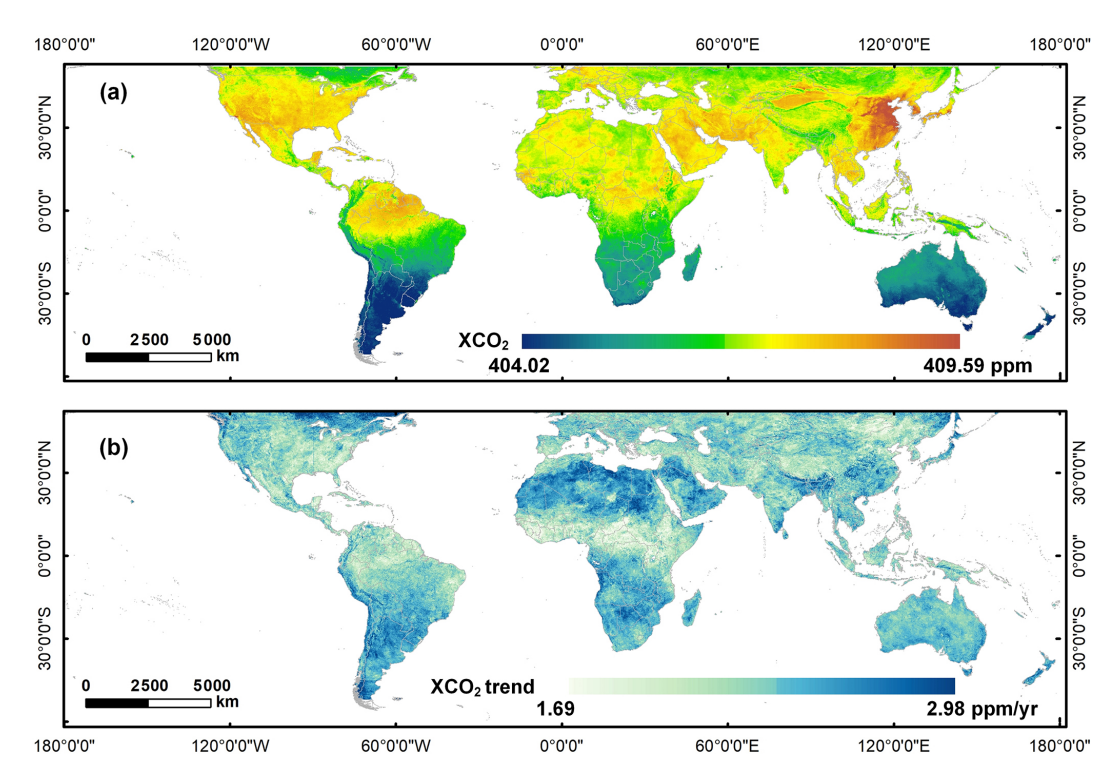


Figure 11. The global spatial distribution of (a) reconstructed 7-year averaged XCO_2 concentration, and (b) its trend from 2015 to 2021 (ppm yr⁻¹ denotes parts per million per year).

accuracy of XCO₂ retrievals. However, our XCO₂ product achieves an optimal balance between spatial detail and measurement precision, exhibiting both high spatial resolution (0.05°) and robust accuracy $(R^2 = 0.91, \text{RMSE} = 1.54 \text{ ppm})$ in comprehensive evaluations.

To evaluate the advancement of our XCO2 product, we compared it with original OCO-2 observations and publicly available global XCO₂ datasets (Wang et al., 2023; Sheng et al., 2022; Zhang et al., 2023) across four regions: North America, Europe with northern Africa, Asia, and Oceania (Fig. 14) in January 2015. Despite monthly aggregation, OCO-2 data exhibit persistent spatial discontinuities, limiting the capacity to analyze monthly XCO2 variability at regional and national scales. Existing XCO₂ products (spatial resolution of 0.25, 1, and 0.1°, respectively) broadly reproduce large-scale XCO₂ patterns but fail to resolve fine-scale heterogeneity. In comparison, our reconstructed XCO2, with the highest spatial resolution, provides a more detailed and accurate representation of the regional XCO2 patterns. For example, lower XCO2 concentrations are clearly identified in eastern Canada (The first row of Fig. 14) and Papua New Guinea (The fourth row of Fig. 14), regions characterized by dense forest cover. This correspondence highlights the substantial carbon sink potential of these forested areas. Our high-resolution product better identifies the CO₂ heterogeneity associated with different land cover types, whereas the coarse-resolution products smooth these signals. This limitation primarily stems from the neglect of high-resolution land cover dynamics and dependence on coarse-resolution assimilated/reanalysis datasets (e.g., CAMS XCO₂, CarbonTracker), resulting in oversmoothed spatial patterns that obscure satellite-derived high-resolution signals. Unlike assimilation-dependent approaches, our method avoids XCO₂ reanalysis inputs, preserving satellite-scale fidelity through high-resolution environmental variables modeling while maintaining precision.

4.2 Limitations and future improvements

Though our XCO₂ products achieved full spatial coverage and high accuracy, however, there are still several limitations need further improvement. In terms of the satellite data, OCO-2 and OCO-3 provide different spatiotemporal coverages. Analyzing OCO-2 and OCO-3 data simultaneously may introduce several uncertainties due to these differences. However, OCO-3 has a similar sensor and inherits the retrieval algorithms of OCO-2. According to Taylor et al. (2023), the mean differences between OCO-3 and OCO-2 are around 0.2 ppm over land. Therefore, we suppose that the discrepancies between their datasets are minimal, and the combined analysis of data from these two satellites will have a negligible impact on our results.

Additionally, though our model integrates multiple environmental variables associated with surface carbon flux vari-

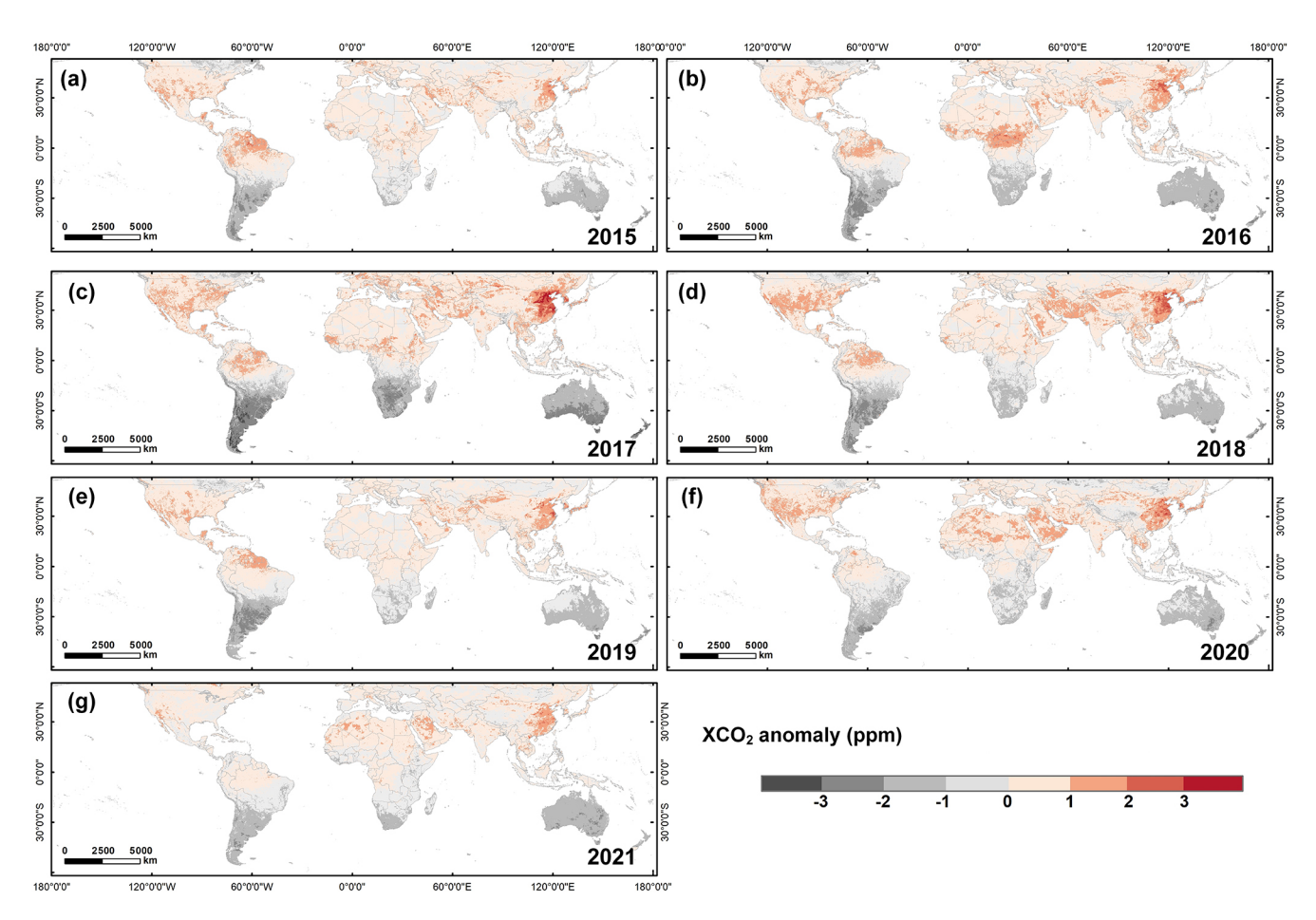


Figure 12. The global spatial distribution of annual XCO₂ anomaly from 2015 to 2021.

Table 6. Comparison between current studies focusing on global XCO₂ reconstruction.

Model	Spatial resolution	In-situ validation (with TCCON)		Reference	
		R^2	RMSE (ppm)	MAE (ppm)	
Attentional-based LSTM	0.05°	0.91	1.54	1.22	Our study
Deep forest	0.1°	0.96	1.01	_	Zhang et al. (2023)
S-STDCT	0.25°	0.95	1.18	_	Wang et al. (2023)
Spatiotemporal kriging	1°	0.97	1.13	0.88	Sheng et al. (2022)
MLE & OI	0.5°	0.92	2.62	1.53	Jin et al. (2022)
ERT	0.01°	0.83	1.79	_	Li et al. (2022)

^{*} S-STDCT: Self-supervised spatiotemporal discrete cosine transform; MLE & OI: maximum likelihood estimation method and optimal interpolation; ERT: Extremely randomized trees.

ations, it does not account for vertical atmospheric transport. As XCO₂ represents the column-averaged CO₂ concentration, vertical redistribution of CO₂ through atmospheric transport (e.g., mixing, convection) can alter the relationship between surface carbon fluxes and column concentrations (Shirai et al., 2012). The absence of such vertical transport indicators may reduce the model's accuracy in regions or pe-

riods with strong vertical mixing. Future efforts will incorporate vertical transport-related variables, such as planetary boundary layer height, vertical wind components, and other reanalysis-derived indicators, to better represent the atmospheric processes that influence the column-averaged CO₂ signal.

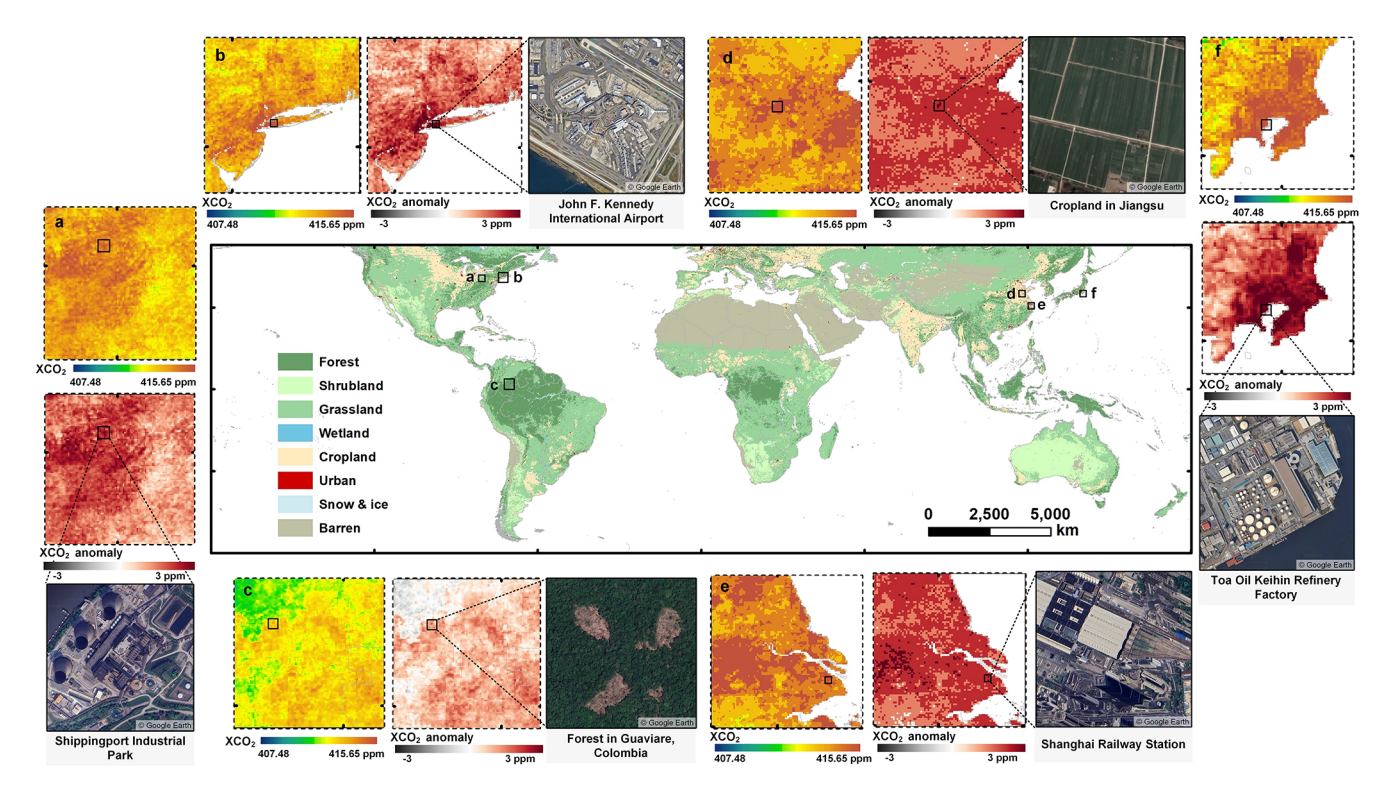


Figure 13. Examples of XCO₂ hotspots in six regions for 2020 detected using the reconstructed products. The subplots present the spatial distribution of XCO₂ concentrations, anomalies (the red panels), and the emission sources (the true color images from © Google Earth), respectively. The global map in the middle presents the land use and land cover types over the globe.

Moreover, while OCO missions currently provide some of the most accurate carbon satellite-based XCO₂ retrievals, they still encounter some retrieval errors and data gaps driven by algorithmic limitations and variable meteorological conditions. A critical research frontier is the refinement of XCO₂ retrieval algorithms to mitigate systematic biases in high-aerosol-load regions (e.g., industrial regions and biomass-burning plumes). Additionally, next-generation hyperspectral satellites, such as the upcoming CO2M (Copernicus Anthropogenic CO₂ Monitoring Mission) with 2 × 2 km² resolution and GeoCarb (Geostationary Carbon Observatory) offering hourly monitoring, will enhance spatial-temporal coverage and reduce cloud-induced data gaps (Reuter et al., 2025).

5 Data availability

The XCO₂ dataset produced in this paper is available at https://doi.org/10.5281/zenodo.12706142 (Wang et al., 2024a). It includes monthly global XCO₂ data at 0.05° resolution, covering the period from December 2014 to December 2021. The dataset is archived in netCDF4 format, with units in parts per million (ppm).

6 Conclusion

As a major driver of global warming, the monitoring of CO₂ changes, especially anthropogenic CO₂ emissions, is of critical importance. The launch of carbon satellites offers a significant advancement for CO₂ monitoring. However, the limited spatial coverage of satellite observations constrains the utility of XCO2 data. While current XCO2 products exhibit relatively high validation accuracy, their coarse spatial resolution remains inadequate for applications such as regionalor county-level emission monitoring, as well as for the detection and inversion of large emission sources. To address these issues, we reconstructed a global full-coverage XCO₂ product at a fine spatial resolution of 0.05° and temporal resolution of 1 month from 2015 to 2021. The advanced deep learning method was adopted to model time-series XCO₂ and incorporate terrestrial flux, anthropogenic flux and climatic impacts into the parameterization process. Through comprehensive evaluations, including cross-validation, insitu validation, spatial distribution assessment and comparison with other XCO₂ products, our reconstructed XCO₂ products demonstrates significant improvements in both accuracy and spatial resolution. The main conclusions and contributions are as following:

1. The advanced At-BiLSTM model could successfully established the nonlinear relationship between satellite-

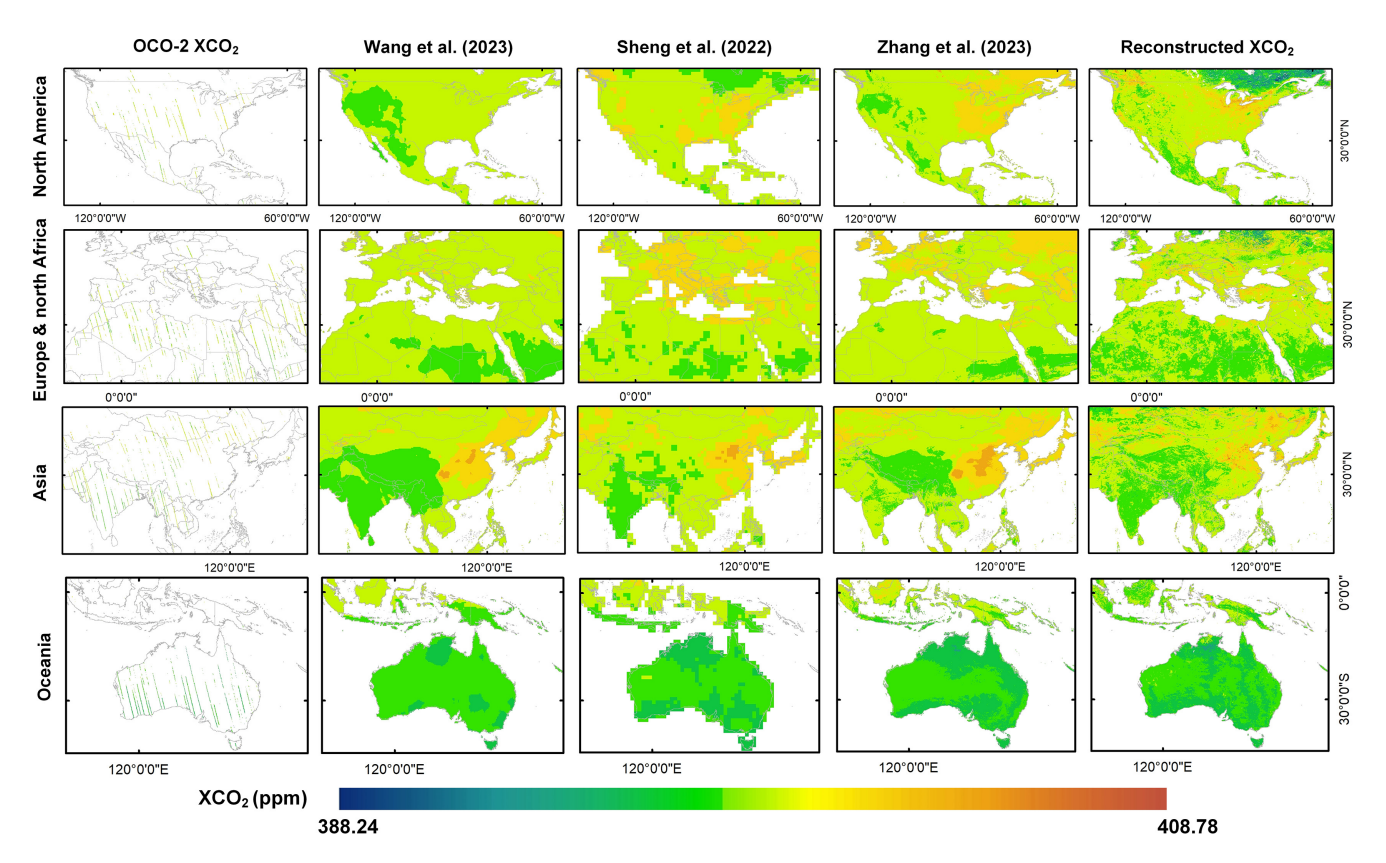


Figure 14. Comparison between the OCO-2 XCO₂ data, accessible XCO₂ products from Wang et al. (2023), Sheng et al. (2022), Zhang et al. (2023), and our reconstructed XCO₂ data in four regions, using the products of January of 2015 as an example.

derived XCO_2 and a set of key environmental variables. And the reconstructed XCO_2 based on our model shows relatively good agreement with TCCON XCO_2 , with R^2 , RMSE, and MAE values of 0.91, 1.58, and 1.22 ppm, respectively.

- 2. The reconstructed XCO₂ product overcomes the extensive data gaps typically caused by narrow satellite swaths and retrieval interference from clouds and aerosols, achieving complete global coverage. Moreover, relative to existing publicly available full-coverage XCO₂ datasets, our product offers the finest spatial resolution (0.05°) while maintaining comparable accuracy.
- 3. Our method avoids coarse XCO₂ reanalysis inputs, preserving satellite-scale fidelity through high-resolution environmental variables modeling. Consequently, the products enable enhanced ability in identifying regional- and county-level XCO₂ hotpots, carbon emissions and fragmented carbon sinks, providing a robust basis for targeted global carbon governance policies.

Author contributions. ZW developed the overall workflow, processed the data and wrote the manuscript. CZ and BH revised the

manuscript. KS, YS, and XC compiled the data. SC conceptualized and revised the manuscript. PA and QZ supervised this study. All the authors contributed to the study.

Competing interests. The contact author has declared that none of the authors has any competing interests.

Disclaimer. Publisher's note: Copernicus Publications remains neutral with regard to jurisdictional claims made in the text, published maps, institutional affiliations, or any other geographical representation in this paper. While Copernicus Publications makes every effort to include appropriate place names, the final responsibility lies with the authors. Also, please note that this paper has not received English language copy-editing.

Acknowledgements. The authors would like to express their gratitude to the NASA Goddard Earth Science Data and Information Services Center for providing the OCO-2/3 XCO₂ products (https://disc.gsfc.nasa.gov/, last access: 11 September 2025), the NASA Land Processes Distributed Active Archive Center (LP DAAC) for providing MODIS data. Our gratitude also goes to the Earth Observation Group (EOG) of the Colorado School of Mines for supplying the NPP-VIIRS NTL products, the European Space Agency (ESA) for providing the TROPOMI data, the Copernicus

Climate Data Store for providing the ERA5 reanalysis data and CAMS-EGG4 XCO₂ data, and the Total Carbon Column Observing Network for their dedication in providing the in situ XCO₂ observations.

Financial support. This work was supported by the Key R&D Program of Zhejiang (grant no. 2022C03078) and National Natural Science Foundation of China (grant no. 32241036).

Review statement. This paper was edited by Bastiaan van Diedenhoven and reviewed by Naveen Chandra and one anonymous referee.

References

- Bahdanau, D., Cho, K., and Bengio, Y.: Neural Machine Translation by Jointly Learning to Align and Translate, arXiv [preprint], https://doi.org/10.48550/arXiv.1409.0473, 19 May 2016.
- Beer, C., Reichstein, M., Tomelleri, E., Ciais, P., Jung, M., Carvalhais, N., Rödenbeck, C., Arain, M. A., Baldocchi, D., Bonan, G. B., Bondeau, A., Cescatti, A., Lasslop, G., Lindroth, A., Lomas, M., Luyssaert, S., Margolis, H., Oleson, K. W., Roupsard, O., Veenendaal, E., Viovy, N., Williams, C., Woodward, F. I., and Papale, D.: Terrestrial Gross Carbon Dioxide Uptake: Global Distribution and Covariation with Climate, Science, 329, 834–838, https://doi.org/10.1126/science.1184984, 2010.
- Bovensmann, H., Burrows, J. P., Buchwitz, M., Frerick, J., Noël, S., Rozanov, V. V., Chance, K. V., and Goede, A. P. H.: SCIAMACHY: Mission Objectives and Measurement Modes, J. Atmos. Sci., 56, 127–150, https://doi.org/10.1175/1520-0469(1999)056<0127:SMOAMM>2.0.CO;2, 1999.
- Buchwitz, M., Reuter, M., Schneising, O., Boesch, H., Guerlet, S., Dils, B., Aben, I., Armante, R., Bergamaschi, P., Blumenstock, T., Bovensmann, H., Brunner, D., Buchmann, B., Burrows, J. P., Butz, A., Chédin, A., Chevallier, F., Crevoisier, C. D., Deutscher, N. M., Frankenberg, C., Hase, F., Hasekamp, O. P., Heymann, J., Kaminski, T., Laeng, A., Lichtenberg, G., De Mazière, M., Noël, S., Notholt, J., Orphal, J., Popp, C., Parker, R., Scholze, M., Sussmann, R., Stiller, G. P., Warneke, T., Zehner, C., Bril, A., Crisp, D., Griffith, D. W. T., Kuze, A., O'Dell, C., Oshchepkov, S., Sherlock, V., Suto, H., Wennberg, P., Wunch, D., Yokota, T., and Yoshida, Y.: The Greenhouse Gas Climate Change Initiative (GHG-CCI): Comparison and quality assessment of near-surface-sensitive satellite-derived CO₂ and CH₄ global data sets, Remote Sens. Environ., 162, 344–362, https://doi.org/10.1016/j.rse.2013.04.024, 2015.
- Butz, A., Guerlet, S., Hasekamp, O., Schepers, D., Galli, A., Aben, I., Frankenberg, C., Hartmann, J.-M., Tran, H., Kuze, A., Keppel-Aleks, G., Toon, G., Wunch, D., Wennberg, P., Deutscher, N., Griffith, D., Macatangay, R., Messerschmidt, J., Notholt, J., and Warneke, T.: Toward accurate CO₂ and CH₄ observations from GOSAT, Geophys. Res. Lett., 38, https://doi.org/10.1029/2011GL047888, 2011.
- Chen, S., Arrouays, D., Leatitia Mulder, V., Poggio, L., Minasny, B., Roudier, P., Libohova, Z., Lagacherie, P., Shi, Z., Hannam, J., Meersmans, J., Richer-de-Forges, A. C., and

- Walter, C.: Digital mapping of *GlobalSoilMap* soil properties at a broad scale: A review, Geoderma, 409, 115567, https://doi.org/10.1016/j.geoderma.2021.115567, 2022.
- Chen, Y., Feng, X., Tian, H., Wu, X., Gao, Z., Feng, Y., Piao, S., Lv, N., Pan, N., and Fu, B.: Accelerated increase in vegetation carbon sequestration in China after 2010: A turning point resulting from climate and human interaction, Glob. Change Biol., 27, 5848–5864, https://doi.org/10.1111/gcb.15854, 2021.
- Crisp, D., Atlas, R. M., Breon, F.-M., Brown, L. R., Burrows, J. P., Ciais, P., Connor, B. J., Doney, S. C., Fung, I. Y., Jacob, D. J., Miller, C. E., O'Brien, D., Pawson, S., Randerson, J. T., Rayner, P., Salawitch, R. J., Sander, S. P., Sen, B., Stephens, G. L., Tans, P. P., Toon, G. C., Wennberg, P. O., Wofsy, S. C., Yung, Y. L., Kuang, Z., Chudasama, B., Sprague, G., Weiss, B., Pollock, R., Kenyon, D., and Schroll, S.: The Orbiting Carbon Observatory (OCO) mission, Adv. Space Res., 34, 700–709, https://doi.org/10.1016/j.asr.2003.08.062, 2004.
- Crisp, D., Pollock, H. R., Rosenberg, R., Chapsky, L., Lee, R. A. M., Oyafuso, F. A., Frankenberg, C., O'Dell, C. W., Bruegge, C. J., Doran, G. B., Eldering, A., Fisher, B. M., Fu, D., Gunson, M. R., Mandrake, L., Osterman, G. B., Schwandner, F. M., Sun, K., Taylor, T. E., Wennberg, P. O., and Wunch, D.: The on-orbit performance of the Orbiting Carbon Observatory-2 (OCO-2) instrument and its radiometrically calibrated products, Atmos. Meas. Tech., 10, 59–81, https://doi.org/10.5194/amt-10-59-2017, 2017.
- Crisp, D., O'Dell, C., Eldering, A., Fisher, B., Oyafuso, F., Payne, V., Drouin, B., Toon, G., Laughner, J., Somkuti, P., McGarragh, G., Merrelli, A., Nelson, R., Gunson, M., Frankenberg, C., Osterman, G., Boesch, H., Brown, L., Castano, R., Christi, M., Connor, B., McDuffie, J., Miller, C., Natraj, V., O'Brien, D., Polonski, I., Smyth, M., Thompson, D., and Granat, R.: Orbiting Carbon Observatory-2&3 (OCO-2 &OCO-3) Level 2 Full Physics Algorithm Theoretical Basis, Tech. Rep. OCO D-55207, NASA Jet Propulsion Laboratory, California Institute of Technology, Pasadena, CA, version 2.0 Rev 3, https://docserver.gesdisc.eosdis.nasa.gov/public/project/OCO/OCO_L2_ATBD.pdf (last access: 11 September 2025), 2021.
- Deng, F., Jones, D. B. A., O'Dell, C. W., Nassar, R., and Parazoo, N. C.: Combining GOSAT XCO₂ observations over land and ocean to improve regional CO₂ flux estimates, J. Geophys. Res.-Atmos., 121, 1896–1913, https://doi.org/10.1002/2015JD024157, 2016.
- Eldering, A., Wennberg, P. O., Crisp, D., Schimel, D. S., Gunson, M. R., Chatterjee, A., Liu, J., Schwandner, F. M., Sun, Y., O'Dell, C. W., Frankenberg, C., Taylor, T., Fisher, B., Osterman, G. B., Wunch, D., Hakkarainen, J., Tamminen, J., and Weir, B.: The Orbiting Carbon Observatory-2 early science investigations of regional carbon dioxide fluxes, Science, 358, eaam5745, https://doi.org/10.1126/science.aam5745, 2017.
- Eldering, A., Taylor, T. E., O'Dell, C. W., and Pavlick, R.: The OCO-3 mission: measurement objectives and expected performance based on 1 year of simulated data, Atmos. Meas. Tech., 12, 2341–2370, https://doi.org/10.5194/amt-12-2341-2019, 2019.
- Friedlingstein, P., Houghton, R. A., Marland, G., Hackler, J., Boden, T. A., Conway, T. J., Canadell, J. G., Raupach, M. R., Ciais, P., and Le Quéré, C.: Update on CO₂ emissions, Nat. Geosci., 3, 811–812, https://doi.org/10.1038/ngeo1022, 2010.

- Friedlingstein, P., O'Sullivan, M., Jones, M. W., Andrew, R. M., Gregor, L., Hauck, J., Le Quéré, C., Luijkx, I. T., Olsen, A., Peters, G. P., Peters, W., Pongratz, J., Schwingshackl, C., Sitch, S., Canadell, J. G., Ciais, P., Jackson, R. B., Alin, S. R., Alkama, R., Arneth, A., Arora, V. K., Bates, N. R., Becker, M., Bellouin, N., Bittig, H. C., Bopp, L., Chevallier, F., Chini, L. P., Cronin, M., Evans, W., Falk, S., Feely, R. A., Gasser, T., Gehlen, M., Gkritzalis, T., Gloege, L., Grassi, G., Gruber, N., Gürses, Ö., Harris, I., Hefner, M., Houghton, R. A., Hurtt, G. C., Iida, Y., Ilyina, T., Jain, A. K., Jersild, A., Kadono, K., Kato, E., Kennedy, D., Klein Goldewijk, K., Knauer, J., Korsbakken, J. I., Landschützer, P., Lefèvre, N., Lindsay, K., Liu, J., Liu, Z., Marland, G., Mayot, N., McGrath, M. J., Metzl, N., Monacci, N. M., Munro, D. R., Nakaoka, S.-I., Niwa, Y., O'Brien, K., Ono, T., Palmer, P. I., Pan, N., Pierrot, D., Pocock, K., Poulter, B., Resplandy, L., Robertson, E., Rödenbeck, C., Rodriguez, C., Rosan, T. M., Schwinger, J., Séférian, R., Shutler, J. D., Skjelvan, I., Steinhoff, T., Sun, Q., Sutton, A. J., Sweeney, C., Takao, S., Tanhua, T., Tans, P. P., Tian, X., Tian, H., Tilbrook, B., Tsujino, H., Tubiello, F., van der Werf, G. R., Walker, A. P., Wanninkhof, R., Whitehead, C., Willstrand Wranne, A., Wright, R., Yuan, W., Yue, C., Yue, X., Zaehle, S., Zeng, J., and Zheng, B.: Global Carbon Budget 2022, Earth Syst. Sci. Data, 14, 4811–4900, https://doi.org/10.5194/essd-14-4811-2022, 2022.
- Gatti, L. V., Basso, L. S., Miller, J. B., Gloor, M., Gatti Domingues, L., Cassol, H. L. G., Tejada, G., Aragão, L. E. O. C., Nobre, C., Peters, W., Marani, L., Arai, E., Sanches, A. H., Corrêa, S. M., Anderson, L., Von Randow, C., Correia, C. S. C., Crispim, S. P., and Neves, R. A. L.: Amazonia as a carbon source linked to deforestation and climate change, Nature, 595, 388–393, https://doi.org/10.1038/s41586-021-03629-6, 2021.
- Gatti, L. V., Cunha, C. L., Marani, L., Cassol, H. L. G., Messias, C. G., Arai, E., Denning, A. S., Soler, L. S., Almeida, C., Setzer, A., Domingues, L. G., Basso, L. S., Miller, J. B., Gloor, M., Correia, C. S. C., Tejada, G., Neves, R. A. L., Rajao, R., Nunes, F., Filho, B. S. S., Schmitt, J., Nobre, C., Corrêa, S. M., Sanches, A. H., Aragão, L. E. O. C., Anderson, L., Von Randow, C., Crispim, S. P., Silva, F. M., and Machado, G. B. M.: Increased Amazon carbon emissions mainly from decline in law enforcement, Nature, 621, 318–323, https://doi.org/10.1038/s41586-023-06390-0, 2023.
- Graves, A. and Schmidhuber, J.: Framewise phoneme classification with bidirectional LSTM and other neural network architectures, Neural Networks, 18, 602–610, https://doi.org/10.1016/j.neunet.2005.06.042, 2005.
- Graves, A., Jaitly, N., and Mohamed, A.: Hybrid speech recognition with Deep Bidirectional LSTM, in: 2013 IEEE Workshop on Automatic Speech Recognition and Understanding, 2013 IEEE Workshop on Automatic Speech Recognition and Understanding, 273–278, https://doi.org/10.1109/ASRU.2013.6707742, 2013.
- Hakkarainen, J., Ialongo, I., and Tamminen, J.: Direct space-based observations of anthropogenic CO₂ emission areas from OCO-2, Geophys. Res. Lett., 43, 11400–11406, https://doi.org/10.1002/2016GL070885, 2016.
- Hammerling, D. M., Michalak, A. M., and Kawa, S. R.: Mapping of CO₂ at high spatiotemporal resolution using satellite observations: Global distributions from OCO-2, J. Geophys. Res.-Atmos., 117, https://doi.org/10.1029/2011JD017015, 2012.

- He, C., Ji, M., Li, T., Liu, X., Tang, D., Zhang, S., Luo, Y., Grieneisen, M. L., Zhou, Z., and Zhan, Y.: Deriving Full-Coverage and Fine-Scale XCO₂ Across China Based on OCO-2 Satellite Retrievals and Carbon-Tracker Output, Geophys. Res. Lett., 49, e2022GL098435, https://doi.org/10.1029/2022GL098435, 2022.
- He, Z., Lei, L., Zhang, Y., Sheng, M., Wu, C., Li, L., Zeng, Z.-C., and Welp, L. R.: Spatio-Temporal Mapping of Multi-Satellite Observed Column Atmospheric CO₂ Using Precision-Weighted Kriging Method, Remote Sens., 12, 576, https://doi.org/10.3390/rs12030576, 2020.
- Hersbach, H., Bell, B., Berrisford, P., Hirahara, S., Horányi, A., Muñoz-Sabater, J., Nicolas, J., Peubey, C., Radu, R., Schepers, D., Simmons, A., Soci, C., Abdalla, S., Abellan, X., Balsamo, G., Bechtold, P., Biavati, G., Bidlot, J., Bonavita, M., De Chiara, G., Dahlgren, P., Dee, D., Diamantakis, M., Dragani, R., Flemming, J., Forbes, R., Fuentes, M., Geer, A., Haimberger, L., Healy, S., Hogan, R. J., Hólm, E., Janisková, M., Keeley, S., Laloyaux, P., Lopez, P., Lupu, C., Radnoti, G., de Rosnay, P., Rozum, I., Vamborg, F., Villaume, S., and Thépaut, J.-N.: The ERA5 global reanalysis, Q. J. Roy. Meteor. Soc., 146, 1999–2049, https://doi.org/10.1002/qj.3803, 2020.
- Hochreiter, S. and Schmidhuber, J.: Long Short-Term Memory, Neural Comput., 9, 1735–1780, https://doi.org/10.1162/neco.1997.9.8.1735, 1997.
- Hubau, W., Lewis, S. L., Phillips, O. L., et al.: Asynchronous carbon sink saturation in African and Amazonian tropical forests, Nature, 579, 80–87, https://doi.org/10.1038/s41586-020-2035-0, 2020.
- IPCC: Climate Change 2023: Synthesis Report. Contribution of Working Groups I, II and III to the Sixth Assessment Report of the Intergovernmental Panel on Climate Change, edited by: Core Writing Team, Lee, H., and Romero, J., IPCC, Geneva, Switzerland, 35–115, https://doi.org/10.59327/IPCC/AR6-9789291691647, 2023.
- Jin, C., Xue, Y., Jiang, X., Zhao, L., Yuan, T., Sun, Y., Wu, S., and Wang, X.: A long-term global XCO₂ dataset: Ensemble of satellite products, Atmos. Res., 279, 106385, https://doi.org/10.1016/j.atmosres.2022.106385, 2022.
- Kemp, L., Xu, C., Depledge, J., Ebi, K. L., Gibbins, G., Kohler, T. A., Rockström, J., Scheffer, M., Schellnhuber, H. J., Steffen, W., and Lenton, T. M.: Climate Endgame: Exploring catastrophic climate change scenarios, P. Natl. Acad. Sci. USA, 119, e2108146119, https://doi.org/10.1073/pnas.2108146119, 2022.
- Li, J., Jia, K., Wei, X., Xia, M., Chen, Z., Yao, Y., Zhang, X., Jiang, H., Yuan, B., Tao, G., and Zhao, L.: High-spatiotemporal resolution mapping of spatiotemporally continuous atmospheric CO₂ concentrations over the global continent, Int. J. Appl. Earth Obs., 108, 102743, https://doi.org/10.1016/j.jag.2022.102743, 2022.
- Lin, B. and Xu, B.: Factors affecting CO₂ emissions in China's agriculture sector: A quantile regression, Renew. Sust. Energ. Rev., 94, 15–27, https://doi.org/10.1016/j.rser.2018.05.065, 2018.
- Liu, G. and Guo, J.: Bidirectional LSTM with attention mechanism and convolutional layer for text classification, Neurocomputing, 337, 325–338, https://doi.org/10.1016/j.neucom.2019.01.078, 2019.
- OCO-2 Science Team/Michael Gunson, Annmarie Eldering: OCO-2 Level 2 bias-corrected XCO₂ and other select fields from the full-physics retrieval aggregated as daily files, Retrospec-

- tive processing V10r, Greenbelt, MD, USA, Goddard Earth Sciences Data and Information Services Center (GES DISC), https://doi.org/10.5067/E4E140XDMPO2, 2020.
- OCO-2/OCO-3 Science Team, Abhishek Chatterjee, Vivienne Payne: OCO-3 Level 2 bias-corrected XCO₂ and other select fields from the full-physics retrieval aggregated as daily files, Retrospective processing v10.4r, Greenbelt, MD, USA, Goddard Earth Sciences Data and Information Services Center (GES DISC), https://doi.org/10.5067/970BCC4DHH24, 2022.
- O'Dell, C. W., Eldering, A., Wennberg, P. O., Crisp, D., Gunson, M. R., Fisher, B., Frankenberg, C., Kiel, M., Lindqvist, H., Mandrake, L., Merrelli, A., Natraj, V., Nelson, R. R., Osterman, G. B., Payne, V. H., Taylor, T. E., Wunch, D., Drouin, B. J., Oyafuso, F., Chang, A., McDuffie, J., Smyth, M., Baker, D. F., Basu, S., Chevallier, F., Crowell, S. M. R., Feng, L., Palmer, P. I., Dubey, M., García, O. E., Griffith, D. W. T., Hase, F., Iraci, L. T., Kivi, R., Morino, I., Notholt, J., Ohyama, H., Petri, C., Roehl, C. M., Sha, M. K., Strong, K., Sussmann, R., Te, Y., Uchino, O., and Velazco, V. A.: Improved retrievals of carbon dioxide from Orbiting Carbon Observatory-2 with the version 8 ACOS algorithm, Atmos. Meas. Tech., 11, 6539–6576, https://doi.org/10.5194/amt-11-6539-2018, 2018.
- Pan, Y., Birdsey, R. A., Fang, J., Houghton, R., Kauppi, P. E., Kurz, W. A., Phillips, O. L., Shvidenko, A., Lewis, S. L., Canadell, J. G., Ciais, P., Jackson, R. B., Pacala, S. W., McGuire, A. D., Piao, S., Rautiainen, A., Sitch, S., and Hayes, D.: A Large and Persistent Carbon Sink in the World's Forests, Science, 333, 988–993, https://doi.org/10.1126/science.1201609, 2011.
- Petzold, A., Thouret, V., Gerbig, C., Zahn, A., Brenninkmeijer, C. A. M., Gallagher, M., Hermann, M., Pontaud, M., Ziereis, H., Boulanger, D., Marshall, J., Nédélec, P., Smit, H. G. J., Friess, U., Flaud, J.-M., Wahner, A., Cammas, J.-P., and Volz-Thomas, A.: Global-scale atmosphere monitoring by in-service aircraft current achievements and future prospects of the European Research Infrastructure IAGOS, Tellus B, 68, 28452, https://doi.org/10.3402/tellusb.v67.28452, 2016.
- Reuter, M., Hilker, M., Noël, S., Di Noia, A., Weimer, M., Schneising, O., Buchwitz, M., Bovensmann, H., Burrows, J. P., Bösch, H., and Lang, R.: Retrieving the atmospheric concentrations of carbon dioxide and methane from the European Copernicus CO2M satellite mission using artificial neural networks, Atmos. Meas. Tech., 18, 241–264, https://doi.org/10.5194/amt-18-241-2025, 2025.
- Sheng, M., Lei, L., Zeng, Z.-C., Rao, W., Song, H., and Wu, C.: Global land 1° mapping dataset of XCO₂ from satellite observations of GOSAT and OCO-2 from 2009 to 2020, Big Earth Data, 7, 170–190, https://doi.org/10.1080/20964471.2022.2033149, 2022.
- Shirai, T., Toshinobu, M., Hidekazu, M., Yousuke, S., Yosuke, N., Shamil, M., and Higuchi, K.: Relative contribution of transport/surface flux to the seasonal vertical synoptic CO₂ variability in the troposphere over Narita, Tellus B, 64, 19138, https://doi.org/10.3402/tellusb.v64i0.19138, 2012.
- Siabi, Z., Falahatkar, S., and Alavi, S. J.: Spatial distribution of XCO₂ using OCO-2 data in growing seasons, J. Environ. Manage., 244, 110–118, https://doi.org/10.1016/j.jenvman.2019.05.049, 2019.
- Sitch, S., Friedlingstein, P., Gruber, N., Jones, S. D., Murray-Tortarolo, G., Ahlström, A., Doney, S. C., Graven, H., Heinze,

- C., Huntingford, C., Levis, S., Levy, P. E., Lomas, M., Poulter, B., Viovy, N., Zaehle, S., Zeng, N., Arneth, A., Bonan, G., Bopp, L., Canadell, J. G., Chevallier, F., Ciais, P., Ellis, R., Gloor, M., Peylin, P., Piao, S. L., Le Quéré, C., Smith, B., Zhu, Z., and Myneni, R.: Recent trends and drivers of regional sources and sinks of carbon dioxide, Biogeosciences, 12, 653–679, https://doi.org/10.5194/bg-12-653-2015, 2015.
- Solomon, S., Plattner, G.-K., Knutti, R., and Friedlingstein, P.: Irreversible climate change due to carbon dioxide emissions, P. Natl. Acad. Sci. USA, 106, 1704–1709, https://doi.org/10.1073/pnas.0812721106, 2009.
- Sundquist, E. T.: Geologic Analogs: Their Value and Limitations in Carbon Dioxide Research, in: Trabalka, J. R. and Reichle, D. E., The Changing Carbon Cycle: A Global Analysis, Springer, New York, 371–402, https://doi.org/10.1007/978-1-4757-1915-4_19, 1986.
- Taylor, T. E., O'Dell, C. W., Frankenberg, C., Partain, P. T., Cronk,
 H. Q., Savtchenko, A., Nelson, R. R., Rosenthal, E. J., Chang,
 A. Y., Fisher, B., Osterman, G. B., Pollock, R. H., Crisp, D., Eldering, A., and Gunson, M. R.: Orbiting Carbon Observatory-2 (OCO-2) cloud screening algorithms: validation against collocated MODIS and CALIOP data, Atmos. Meas. Tech., 9, 973–989, https://doi.org/10.5194/amt-9-973-2016, 2016.
- Taylor, T. E., Eldering, A., Merrelli, A., Kiel, M., Somkuti, P., Cheng, C., Rosenberg, R., Fisher, B., Crisp, D., Basilio, R., Bennett, M., Cervantes, D., Chang, A., Dang, L., Frankenberg, C., Haemmerle, V. R., Keller, G. R., Kurosu, T., Laughner, J. L., Lee, R., Marchetti, Y., Nelson, R. R., O'Dell, C. W., Osterman, G., Pavlick, R., Roehl, C., Schneider, R., Spiers, G., To, C., Wells, C., Wennberg, P. O., Yelamanchili, A., and Yu, S.: OCO-3 early mission operations and initial (vEarly) XCO₂ and SIF retrievals, Remote Sens. Enviro., 251, 112032, https://doi.org/10.1016/j.rse.2020.112032, 2020.
- Taylor, T. E., O'Dell, C. W., Baker, D., Bruegge, C., Chang, A., Chapsky, L., Chatterjee, A., Cheng, C., Chevallier, F., Crisp, D., Dang, L., Drouin, B., Eldering, A., Feng, L., Fisher, B., Fu, D., Gunson, M., Haemmerle, V., Keller, G. R., Kiel, M., Kuai, L., Kurosu, T., Lambert, A., Laughner, J., Lee, R., Liu, J., Mandrake, L., Marchetti, Y., McGarragh, G., Merrelli, A., Nelson, R. R., Osterman, G., Oyafuso, F., Palmer, P. I., Payne, V. H., Rosenberg, R., Somkuti, P., Spiers, G., To, C., Weir, B., Wennberg, P. O., Yu, S., and Zong, J.: Evaluating the consistency between OCO-2 and OCO-3 XCO₂ estimates derived from the NASA ACOS version 10 retrieval algorithm, Atmos. Meas. Tech., 16, 3173–3209, https://doi.org/10.5194/amt-16-3173-2023, 2023.
- Wang, Z., Hu, B., Huang, B., Ma, Z., Biswas, A., Jiang, Y., and Shi, Z.: Predicting annual PM_{2.5} in mainland China from 2014 to 2020 using multi temporal satellite product: An improved deep learning approach with spatial generalization ability, ISPRS J. Photogramm., 187, 141–158, https://doi.org/10.1016/j.isprsjprs.2022.03.002, 2022.
- Wang, Y., Yuan, Q., Li, T., Yang, Y., Zhou, S., and Zhang, L.: Seamless mapping of long-term (2010–2020) daily global XCO₂ and XCH₄ from the Greenhouse Gases Observing Satellite (GOSAT), Orbiting Carbon Observatory 2 (OCO-2), and CAMS global greenhouse gas reanalysis (CAMS-EGG4) with a spatiotemporally self-supervised fusion method, Earth Syst. Sci. Data, 15, 3597–3622, https://doi.org/10.5194/essd-15-3597-2023, 2023.

- Wang, Z., Zhang, C., Shi, K., Shangguan, Y., Hu, B., Chen, X., Wei, D., Chen, S., Atkinson, P., and Zhang, Q.: A monthly full-coverage satellite-based global atmospheric CO₂ dataset at 0.05° resolution from 2015 to 2021, Zenodo [data set], https://doi.org/10.5281/zenodo.12706142, 2024a.
- Wang, Z., Zhang, C., Ye, S., Lu, R., Shangguan, Y., Zhou, T., Atkinson, P. M., and Shi, Z.: Tracking hourly PM_{2.5} using geostationary satellite sensor images and multiscale spatiotemporal deep learning, Int. J. Appl. Earth Obs., 134, 104145, https://doi.org/10.1016/j.jag.2024.104145, 2024b.
- Wunch, D., Toon, G. C., Wennberg, P. O., Wofsy, S. C., Stephens,
 B. B., Fischer, M. L., Uchino, O., Abshire, J. B., Bernath, P.,
 Biraud, S. C., Blavier, J.-F. L., Boone, C., Bowman, K. P., Browell, E. V., Campos, T., Connor, B. J., Daube, B. C., Deutscher,
 N. M., Diao, M., Elkins, J. W., Gerbig, C., Gottlieb, E., Griffith, D. W. T., Hurst, D. F., Jiménez, R., Keppel-Aleks, G., Kort,
 E. A., Macatangay, R., Machida, T., Matsueda, H., Moore, F.,
 Morino, I., Park, S., Robinson, J., Roehl, C. M., Sawa, Y., Sherlock, V., Sweeney, C., Tanaka, T., and Zondlo, M. A.: Calibration of the Total Carbon Column Observing Network using aircraft profile data, Atmos. Meas. Tech., 3, 1351–1362, https://doi.org/10.5194/amt-3-1351-2010, 2010.
- Wunch, D., Toon, G. C., Blavier, J.-F. L., Washenfelder, R. A., Notholt, J., Connor, B. J., Griffith, D. W. T., Sherlock, V., and Wennberg, P. O.: The Total Carbon Column Observing Network, Philos. T. R. Soc. A, 369, 2087–2112, https://doi.org/10.1098/rsta.2010.0240, 2011.
- Wunch, D., Wennberg, P. O., Osterman, G., Fisher, B., Naylor, B., Roehl, C. M., O'Dell, C., Mandrake, L., Viatte, C., Kiel, M., Griffith, D. W. T., Deutscher, N. M., Velazco, V. A., Notholt, J., Warneke, T., Petri, C., De Maziere, M., Sha, M. K., Sussmann, R., Rettinger, M., Pollard, D., Robinson, J., Morino, I., Uchino, O., Hase, F., Blumenstock, T., Feist, D. G., Arnold, S. G., Strong, K., Mendonca, J., Kivi, R., Heikkinen, P., Iraci, L., Podolske, J., Hillyard, P. W., Kawakami, S., Dubey, M. K., Parker, H. A., Sepulveda, E., García, O. E., Te, Y., Jeseck, P., Gunson, M. R., Crisp, D., and Eldering, A.: Comparisons of the Orbiting Carbon Observatory-2 (OCO-2) XCO₂ measurements with TCCON, Atmos. Meas. Tech., 10, 2209–2238, https://doi.org/10.5194/amt-10-2209-2017, 2017.

- Yuan, Q., Shen, H., Li, T., Li, Z., Li, S., Jiang, Y., Xu, H., Tan, W., Yang, Q., Wang, J., Gao, J., and Zhang, L.: Deep learning in environmental remote sensing: Achievements and challenges, Remote Sens. Environ., 241, 111716, https://doi.org/10.1016/j.rse.2020.111716, 2020.
- Zeng, N., Zhao, F., Collatz, G. J., Kalnay, E., Salawitch, R. J., West, T. O., and Guanter, L.: Agricultural Green Revolution as a driver of increasing atmospheric CO₂ seasonal amplitude, Nature, 515, 394–397, https://doi.org/10.1038/nature13893, 2014.
- Zhang, L., Li, T., Wu, J., and Yang, H.: Global estimates of gap-free and fine-scale CO₂ concentrations during 2014–2020 from satellite and reanalysis data, Environ. Int., 178, 108057, https://doi.org/10.1016/j.envint.2023.108057, 2023.
- Zhang, M. and Liu, G.: Mapping contiguous XCO₂ by machine learning and analyzing the spatio-temporal variation in China from 2003 to 2019, Sci. Total Environ., 858, 159588, https://doi.org/10.1016/j.scitotenv.2022.159588, 2023.